5-2014

Particle Image Velocimetry (PIV) for Positron Emission Particle Tracking (PEPT) and Turbulence Modeling Validation

Sarah Ridley Rupert
University of Tennessee - Knoxville, srupert@utk.edu

To the Graduate Council:

I am submitting herewith a thesis written by Sarah Ridley Rupert entitled "Particle Image Velocimetry (PIV) for Positron Emission Particle Tracking (PEPT) and Turbulence Modeling Validation." I have examined the final electronic copy of this thesis for form and content and recommend that it be accepted in partial fulfillment of the requirements for the degree of Master of Science, with a major in Nuclear Engineering.

Arthur E. Ruggles, Major Professor

We have read this thesis and recommend its acceptance:

Lawrence H. Heilbronn, Eric D. Lukosi

Accepted for the Council:
Carolyn R. Hodges

Vice Provost and Dean of the Graduate School

(Original signatures are on file with official student records.)

Particle Image Velocimetry (PIV) for Positron Emission Particle Tracking (PEPT) and Turbulence Modeling Validation

A Thesis Presented for the
Master of Science
Degree
The University of Tennessee, Knoxville

Sarah Ridley Rupert
May 2014

ACKNOWLEDGEMENTS

I would like to thank Dr. Arthur Ruggles for the opportunity to work on this project, and his guidance throughout my undergraduate and graduate school career. My work could not have been completed without the funding of the NNSA and the privilege to use the Post 9/11 G.I. Bill. I would also like to thank my family for their continued support throughout my education.

ABSTRACT

A Particle Image Velocimetry (PIV) experiment is designed and data collected with intention to validate Positron Emission Particle Tracking (PEPT) methods. The PIV data are collected in a narrow rectangular channel for flow Reynolds number near 20,000. The narrow channel and attendant pump, header tanks and flow instrumentation are portable and designed to allow identical tests in a Concord Microsystems MicroPET P4 pre-clinical PET scanner at the pre-clinical Imaging Suite at the UT Hospital. The PIV data are instantaneous velocity field data, allowing statistics on the flow turbulence to be collected in the Eulerian frame. The PEPT method measures activated particle trajectories in time, corresponding to a Lagrangian measurement. The relationship between the PIV data collected herein, and the anticipated PEPT data is explored to provide a path for validating the performance of the PEPT method for flow measurement. The utility of the PEPT method extends to opaque fluids and flow in complex and opaque flow boundaries. These flow conditions are impossible or technically difficult for optical PIV methods to address. The PEPT method also provides full 4 dimensional particle trajectory data, with temporal and spatial resolution competitive with the most advanced optical PIV methods.

TABLE OF CONTENTS

LIST OF TABLES

LIST OF FIGURES

NOMENCLATURE

ρ	Density
L_c	Characteristic Length
U	Velocity
μ	Dynamic Viscosity
ν	Kinematic Viscosity
Re	Reynolds Number
d_h	Hydraulic Diameter
A_{xs}	Cross-Sectional Area
P_w	Wetted Perimeter
Pr	Prandtl Number
d	Diameter
T	Turbulence Intensity
t	Time
D	Diffusion Coefficient

CHAPTER 1

INTRODUCTION AND GENERAL INFORMATION

1.1 Opportunity

Particle tracking to infer flow velocity profiles in turbulent conditions is important to a number of engineering applications. Flow and mixing in nuclear reactors, food processing equipment, nuclear fuel reprocessing equipment, and materials separation processes involve opaque fluids and structures. Optical methods are well-developed, but restrict investigation to optically clear environments. Positron emission particle tracking (PEPT) offers particle tracking capability in opaque environments and fluids, and in turn provides information of velocity profiles and flow turbulence. While significant prior use of PEPT can be found in the literature, a direct comparison of PEPT to well established optical particle image velocimetry (PIV) methods is not available. PIV can be used to validate the capabilities of PEPT as a particle tracking method suited to opaque fluids and structures. This research is part of a radiochemistry center funded by NNSA as part of the Stockpile Stewardship Academic Partners Program.

1.2 Background

Current PIV data acquisition requires a transparent environment to measure velocity fields, excluding it as an option for the investigation of opaque fluids and structures. Particles in the flow are illuminated by two laser pulses, separated by a timing window. A camera records a set of images, one for each of the two pulses, and PIV processing software uses the particle displacements between the two images to develop an Eulerian description of the particle movements. A sufficiently large group of image sets will offer a description of the velocity flow field, including the time averaged velocity field and statistics on time varying components attributable to turbulence.

The PEPT method utilizes gamma radiation detection and PET technology to track particle movement, rendering PEPT a viable method of particle tracking in opaque environments. PEPT provides a three dimensional Lagrangian description of the flow by following the trajectory of the particle in time. The positron-electron annihilation creates twin gammas nearly 180 degrees opposed in trajectory. Detection of coincident gamma ray pairs establishes a line of response (LOR) passing through or very near the particle. The stream of coincident counts establishes the evolution of LORs passing through the particle trajectory in the flow. A velocity field and flow turbulence information over the interrogation volume can be interpolated from a number of measured particle trajectories.

PIV divides a two dimensional interrogation plane into several regions and assigns each region an averaged velocity value descriptive of the velocity of all

particles in that region. These velocity values at specific locations result in an Eulerian description of the flow field. A series of single-exposed images acquired with PIV over a sufficiently long time will allow for reconstruction of a Langrangian description of the flow field.

An experiment is designed that allows for PIV and PEPT data acquisition for identical flow conditions. The comparison will provide a validation of the PEPT measurement approach and confirm or extend claimed uncertainties in the PEPT method. The inconsistency in flow field specifications between PIV and PEPT require an investigation of the theoretical and statistical relationship between Lagrangian and Eulerian data. The author does not have the background to facilitate a thorough understanding of this relationship, but beginning research is offered on this topic and that provides references for future study.

1.3 Thesis Outline

Designing an experiment to validate PEPT requires an understanding of both turbulent flow theory and the PET scanner performance. Chapter 2.1 addresses the basic science of turbulent flow and the properties of an internal boundary layer. Chapter 2.2 gives an extensive overview of PET, and Chapter 2.3 describes the combination of 2.1 and 2.2 into the PEPT method and gives a review of prior applications of the PEPT method. Chapter 2.4 overviews the PIV method as a PEPT validation technique, and Chapter 2.5 introduces the Eulerian and Lagrangian relationship between the two methods.

Chapter 3 and 4 describe the 1st and 2nd PIV experiments respectively, including improvements made to obtain better statistics. Chapter 5 describes the PEPT experiment, and Chapter 6 offers conclusions and future work.

CHAPTER 2

LITERATURE REVIEW

2.1 Turbulence and Boundary Layer Theory

The Reynolds number characterizes a duct's turbulence and fluid boundary layer using a ratio of the flow inertial force over viscous force.

$$Re = \frac{inertia}{viscous} = \frac{\rho L_c^3 U^2 / L_c}{\mu L_c^2 U / L_c} = \frac{U L_c}{\nu}$$

In a duct the characteristic length, L_c, is described by the hydraulic diameter, d_h, of the duct.

$$d_h = \frac{4A_{xs}}{P_w}$$

The transition Reynolds number is a function of several parameters, including roughness, but is generally accepted as near 2300. If the Re of the flow

is higher than the transition number, near 10,000, the flow is turbulent. Turbulent flow is characterized by random, fluctuating motion, superimposed on the time averaged velocity components. Viscous effects are negligible in comparison to the inertial forces in the fluid when the flow is fully turbulent, as characterized by a Re of at least 10,000.

2.1.1 *Internal Boundary Layer*

A duct's internal fluid boundary layer has several characteristics. Each interface between the duct wall and the fluid has a no slip condition where the fluid has zero velocity. Reactive drag stresses in the direction of fluid motion oppose the viscous shear stresses between the fluid and duct walls. These stresses cause a loss in fluid momentum and result in a velocity variation in the direction normal to the wall. A separate boundary layer forms on each wall and grows until they all meet in the center of the duct. Figure 1 depicts the boundary layer structure in an turbulent internal flow.

The viscous effects are dominant in the sublayer closest to the wall of the duct. Viscous effects still dominate in the buffer layer, just above the viscous sublayer, but turbulence becomes more significant. The turbulence effects increase through the overlap layer into the turbulent layer where the turbulent effects dominate.

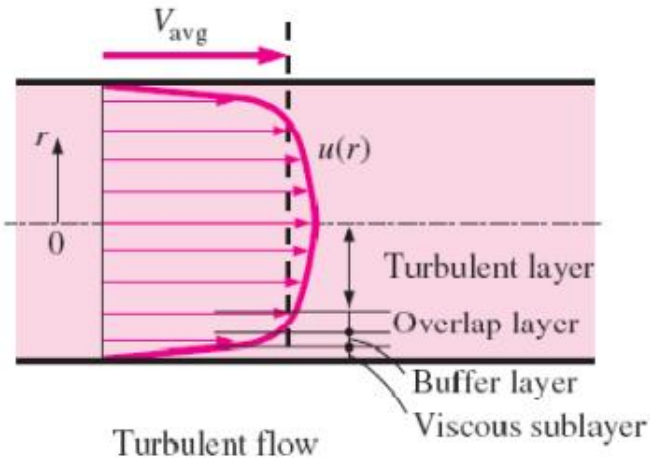

Figure 1: Turbulent Boundary Layers[2]

The thermal boundary layer is identical to the fluid boundary layer when the Prandtl number, $\frac{\nu}{\alpha}$, is near unity. Prandtl number is near unity for air and warm water. The entrance length, L_e, is the distance in the flow direction at which the flow is fully developed, where the velocity profile becomes invariant. For a turbulent flow, the $L_e \approx 4.40(d)Re^{1/6}$, or 23.2 hydraulic diameters with a Re of 20,000.

2.1.2 *Navier-Stokes*

A velocity flow field is mathematically described by a solution to Navier-Stokes equations, characterized by velocity (***u***), density (ρ), pressure (p), deviatoric component of the stress tensor (**T**), and body forces (**f**).

$$\rho\left(\frac{\partial \overline{\boldsymbol{u}}}{\partial t} + \boldsymbol{u}\cdot\nabla\boldsymbol{u}\right) = -\nabla p + \nabla\cdot\boldsymbol{T} + \boldsymbol{f}$$

The variable behavior over time in turbulent flow presents an extremely difficult solution to the equations, and prompts the use of reduced order turbulence models such as Reynolds-averaged Navier-Stokes (RANS) or Large eddy simulation (LES).Turbulent instantaneous velocities are divided into a time-averaged component and a fluctuating component:

$$\vec{\boldsymbol{u}} = \vec{\bar{u}} + \vec{u'}$$

The root mean squared velocity describes the magnitude of an instantaneous velocity vector and is defined as:

$$u_{i,rms} = \sqrt{u_i'(x,y)^2}$$

A RANS model is thus described as:

$$\rho\bar{u}_j\frac{\partial \bar{u}_\iota}{\partial x_j} = \rho\bar{f}_\iota + \frac{\partial}{\partial x_j}\left[-\bar{p}\delta_{ij} + \mu\left(\frac{\partial \bar{u}_\iota}{\partial x_j} + \frac{\partial \bar{u}_j}{\partial x_i}\right) - \rho\overline{u_\iota' u_j'}\right]$$

Note that the Reynolds averaged mean velocity, $\bar{u}$, does not provide a directional description of the instantaneous velocity. *An individual particle trajectory cannot be predicted using the time averaged velocity values*.

2.1.3 *Turbulence Intensity*

Turbulence intensity, *T,* characterizes the level of turbulence in a flow in terms of percent. In general form the turbulence intensity is a ratio of the root mean squared velocity to the Reynolds averaged mean velocity,[4]

$$T_{u_i} = \frac{u_{i,rms}(x,y)}{U_i}.$$

Geometry and flow speed determine whether flow turbulence is categorized as high, medium, or low intensity. Simple geometries and low flow speeds, as within the context of this paper, indicate medium turbulence intensity, estimated as $T = 0.16Re_{d_h}^{-\frac{1}{8}}$.[3] At the center of fully developed, medium-turbulence environments, intensities generally range from one to five percent.

2.2 Positron Emission Tomography (PET)

PET is a well-developed technique most often utilized in a medical environment. The method uses twin gamma rays emitted from a positron annihilation with an electron to form 3D images of the activity field. Positron emitter Fluorine, F-18, is attached to a glucose molecule, Fludeoxyglucose (FDG), for use in most medical PET imaging applications. The FDG is preferentially metabolized by tumors, allowing an image of these malignancies.

2.2.1 *Positron Emission and Annihilation*

A nucleus made unstable by too many protons will convert a proton into a neutrally charged neutron by emitting a positively charged positron and a neutrino. The positron is the antiparticle to the electron, and originates from beta plus decay;

$$^{A}_{Z}X \rightarrow {}_{Z-1}{}^{A}Y + \beta^{+} + \upsilon + energy$$

After release from the nucleus, the positron will approach thermal energy over a distance dependent on the positron energy and the transport medium. The distance for positrons emitted from F-18 , the isotope to be used in these studies, is typically 2 mm in water and 0.5 mm in steel. In gaseous mediums the distance could be tens of centimeters. The positron range limits the resolution of a PET scanner.[5] When the positron achieves thermal energy it can annihilate with an electron or bond with and electron forming positronium. The lifetime of positronium is on the average of picoseconds. Positronium decay also results in twin coincident gammas and a neutrino. Upon annihilation, the rest mass in the annihilation frame is instantaneously converted to energy in the form of two coincident, 511 keV annihilation photons.[6]

Electric charge, angular momentum, total energy, and linear momentum must all be conserved in the annihilation process. In the case of formation of positronium, the momentum distribution between the positronium and a condensed matter can describe details of the substrate structure.[7] A Feynman diagram illustrating the annihilation process is shown in Figure 1.

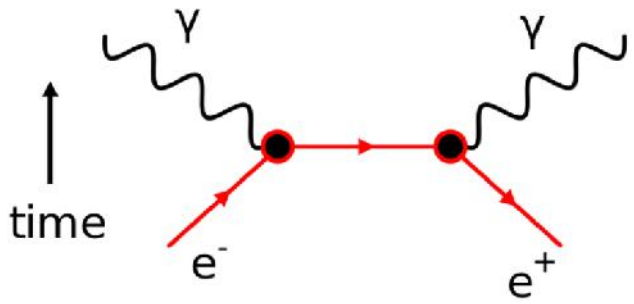

Figure 2: Feynman Diagram

Once annihilation occurs, the scanner detectors record coincident photons along a line of response assuming the photons are emitted 180 degrees from each other. A collection of several million LORs is used to create a 3-D image of activity, a positron emission tomograph.

2.2.2 *Effects on Scanner Resolution*

The resolution of the scanner determines the precision to which a particle can be located. The scanner resolution is a balance between intrinsic resolution and reducing the image variance.[8] The scanner detector type determines the intrinsic resolution, or the best possible resolution, which is typically less than 5 mm for clinical models. However, the true, or reconstructed, resolution is closer to 8 mm as determined by imaging of standard activity fields such as the Derenzo Phantom. Variance is determined by the number of counts the detector receives to be used in image reconstruction. Hence radionuclide activity, scanner sensitivity, scanner count-rate capability, and duration of the scan are the factors that contribute to image variance.

When two photons are detected within the coincidence timing window, a true coincidence event is recorded determining a line-of-response between the two detectors. A true coincidence event assumes that neither photon was scattered.[8] Ideally, all photons would be detected 180 degrees opposed by the detectors. In reality there is a non-collinearity governed by the positron and electron momentum when they annihilate. This component of uncertainty grows with the diameter of the scanner bore, and is a dominant contributor of uncertainty for F-18 imaging in modern clinical scanners.

The photon also has the potential to be altered due to interaction before reaching the detectors. The predominant mechanism for photon interaction is dictated by the photon energy and the atomic number of the material with which the photons are interacting. Figure 3 shows the interaction mechanism as a function of atomic number and photon energy.

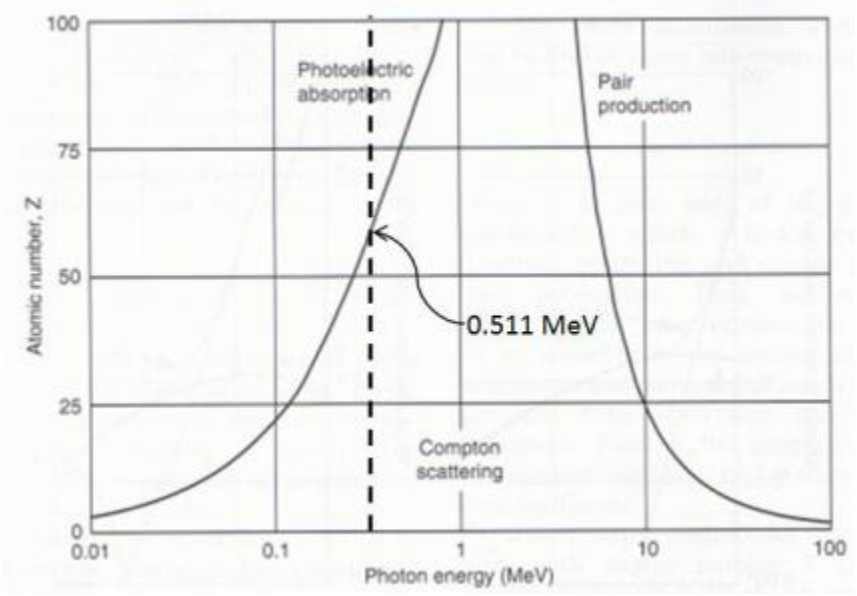

Figure 3: Photon Interaction Possibilities as a Function of Energy and Atomic Number of Interactive Material. [8]

Compton Scattering and photoelectric absorption are possible at 511 keV as seen in Figure 3. Photoelectric absorption is negligible at low atomic numbers. When Compton Scattering occurs, the counting efficiency of the PET scanner is adversely affected. Between the point of annihilation and the detector, a photon may interact with charged particles, such as an electrons. Maintaining the conservation of energy and momentum, these interactions result in the photon losing energy and changing direction. The correct LOR will be lost if one of the coincident photons is scattered.

The probability that a photon will not interact with another particle before reaching the detector is called the survival probability, $P_{d\theta}$, and is a function of the linear attenuation coefficient at a position x, $\mu(x)$. The survival probability is defined as:

$$P_{d\theta} = \exp\left[\int_l \mu(x)dx\right]$$

Such attenuation will cause a significant variation in reconstructed image activity density across the FOV, with the lowest intensity in the centre of the image.[9] Correction for attenuation is important during image reconstruction, and has led to integration of gamma computed tomography (CT) measurements with PET scanners.

A scattered event is measured when the scattered photons do not escape the FOV, but are detected off the true LOR. This will add error to the data.[8] Applying an energy threshold to the detected gammas can help differentiate scattered and non-scattered photons because scattering will cause the photons to lose energy.

Random, or accidental, coincidence events are also possible. A scanner detector ring subtends a small solid angle in relation to the high number of scattered photons, leading to many cases of only one photon of the pair being detected. These detected photons are known as singles, but if two singles, originating from different annihilation events are detected within the same coincidence timing window they will be recorded as a coincidence event, with an incorrect corresponding LOR. Decreasing the timing window reduces the number of accidental coincidences. Variation in rise-time of crystal light output govern the minimum timing window possible. The crystal response depends on the type of crystal material being used in the detector. The accidental coincidence rate increases as the square of the amount of the radionuclide in the FOV. Figure 4

illustrates the detection inaccuracy caused by scattering and random events.[8] The dotted line represents the recorded LOR.

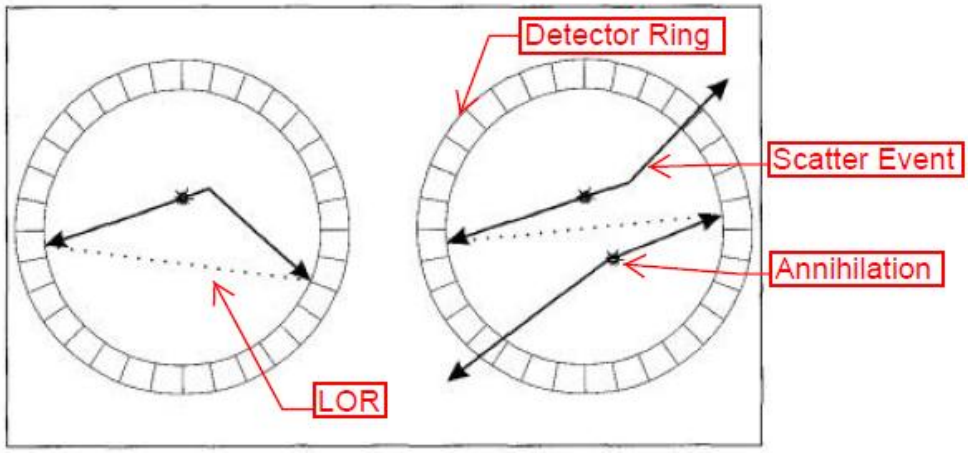

Figure 4: Scattered Photon Detection Errors[8]

When a detector is processing an event, it cannot record a new event. This processing time is known as dead time. As the number of counts per unit time increases, the random events and true events both saturate the scanner. To avoid this, the dose from the radionuclide must be low enough to keep the number of counts below the maximum count-rate capability of the scanner.

The detector material and size are very important in determining PET resolution. Using more and smaller crystals increases the spatial resolution of the reconstructed image. A faster scintillator will provide a higher count-rate capability, and a higher energy threshold will improve the energy resolution by

ruling out more scattered events. Figure 5 demonstrates the scatter fraction as a function of energy threshold, scintillation material, and object size.

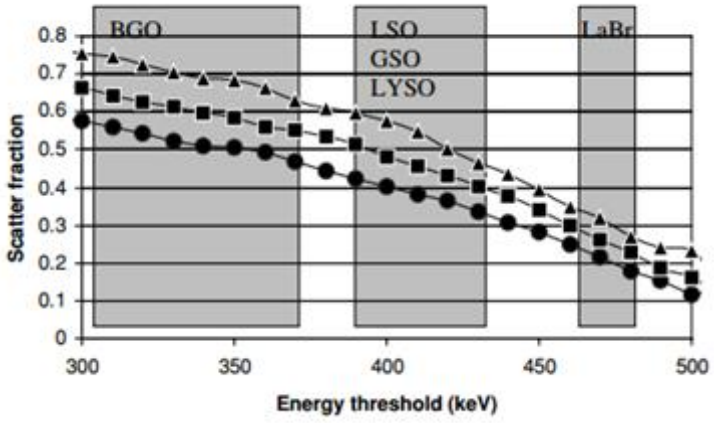

Figure 5: Scatter Fraction as a Function of Energy for Several Scintillator Materials. Circles, squares, and triangles represent an object size of 20 cm, 27 cm and 35 cm respectively.[8]

2.2.3 *Reconstruction*

Backprojection is the most common process used to reconstruct a tomographic image. Each detected annihilation event records coordinates in the respective detectors between which a LOR can be drawn. The number of photon pairs detected along a LOR is proportional to the activity along that LOR. In 3D PET scans, the interrogation volume is divided into voxels. The "occupancy" of each voxel is increased as a new LOR passes through that voxel. Because there is no way to know where along the LOR the annihilation took place, the backprojected image is blurred. A backprojected image of a known point source can be used to develop a point spread function (PSF), and then used to

deconvolve the original image in Fourier space, or comparable method.[10] A large number of counts and corresponding LORs are needed to obtain a reliable image.

2.2.4 *Tracers*

Radionuclide choice is also important in the PET technique. Table 1 lists radionuclides that are commonly used as PET tracers. The best radionuclide for the purpose of medical PET has half-life long enough to allow distribution to several hospitals and associated PET scanners, but short enough to minimize the cumulative dose to a patient due to the imaging. Fluorine-18 (F-18) fulfills these requirements and has become a widely used radiopharmaceutical when tagged to fluorodeoxyglucose (FDG).[9] The attractiveness of PET has grown dramatically over the past two decades as the availability and distribution of FDG has expanded to all major cities. Now each PET scanner need not be accompanied by an on-site cyclotron to provide F-18.

Table 1: Common Radionuclides Used as PET Tracers[9]

Nuclide	Half life	β^+ decay fraction	Production route
^{82}Rb	78 s	0.96	from ^{82}Sr generator
^{15}O	122 s	1	$^{14}N(d,n)^{15}O$
^{13}N	10 min	1	$^{12}C(d,n)^{13}N$
^{11}C	20.3 min	1	$^{14}N(p,\alpha)^{11}C$
^{68}Ga	68 min	0.9	From ^{68}Ge generator
^{18}F	110 min	1	$^{18}O(p,n)^{18}F$ or $^{16}O(^3He,p)^{18}F$ and $^{16}O(^3He,n)^{18}Ne \rightarrow ^{18}F$
^{45}Ti	3.1 h	0.86	$^{45}Sc(p,n)^{45}Ti$
$^{62}Zn/^{62}Cu$	9.2 h	0.98	$^{63}Cu(p,2n)^{62}Zn$
^{66}Ga	9.7h	0.57	$^{66}Zn(p,n)^{66}Ga$
^{64}Cu	12.7 h	0.19	$^{64}Ni(d,2n)^{64}Cu$ or $^{63}Cu(n,\gamma)^{64}Cu$
$^{140}Nd/^{140}Pr$	3.4 days	0.49	$^{141}Pr(p,2n)^{140}Nd$
^{124}I	4.2 days	0.25	$^{124}Te(d,2n)^{124}I$
$^{82}Sr/^{82}Rb$	25 days	0.96	Abundant fission product
$^{68}Ge/^{68}Ga$	271 days	0.9	$^{66}Zn(\alpha,2n)^{68}Ge$
^{22}Na	2.6 years	0.9	$^{24}Mg(d,\alpha)^{22}Na$

2.3 Positron Emission Particle Tracking

The PEPT method combines PET and fluid flow physics. The method utilizes the PET scanner to track the motion of a single active tracer particle in a fluid.[5] Knowing there is only one particle in the FOV, PET can be used to map the position and velocity of the particle in a Lagrangian frame of reference.

2.3.1 *PEPT Overview*

Particle image velocimetry and variants are the leading methods of mapping velocity profiles and turbulent flow mixing. However, these methods are

limited to environments that are optically clear. There is need for an investigative method in opaque fields. Fifty percent of photons from an activated particle will travel through 11 mm of steel, demonstrating that PET can be used to study processes outside the medical field, such as flows in process applications and equipment.[11]

In non-medical applications, patient dose is not a concern, though operator dose is, and the list of applicable radionuclides can be increased.

A 1 MeV positron in materials of typical densities[12] can be expected to annihilate within 1 mm from emission so when detectors within a PET scanner detect coincident gamma rays, it can be inferred positron emission occurred along the corresponding chord between the two detectors.[12] The minimum distance point for a set of trajectories is the point that minimizes the sum of perpendicular distances to the trajectories, and the point in the FOV closest to which all the trajectories for a given set of events passes.[13] This is the point that defines the particle's location, as depicted in Figure 6.

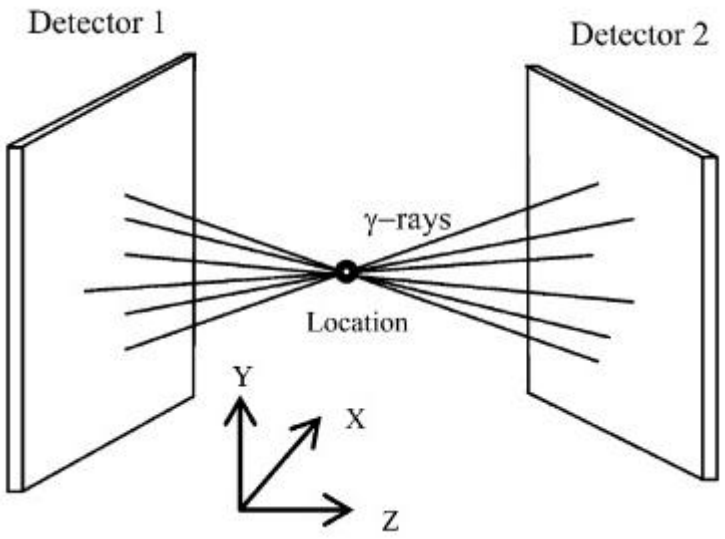

Figure 6: Schematic Diagram of PEPT for a Single Particle[13]

Ideally, an infinite number of chords could be mapped to provide an exact location of the tracer particle in the working fluid. However, there is a maximum particle specific activity that can be achieved, and a maximum number of coincidence counts that can be recorded in a given period of time. These factors limit the precision for particle location.

Compton scattering can also induce error in particle location, and even unscattered annihilation photons are not exactly 180 degrees opposed. Because of the deviation in photon opposition, not all coincident gammas detected will have originated from the same particle location. A group at the University of Birmingham developed an algorithm for discarding gamma ray trajectories with LOR that pass far from the activated particle. The remaining trajectories are then used to map a three dimensional, slow moving particle location to within 1mm several times per second. They found that approximately 100 events are

necessary to obtain legitimate statistics, and that small, neutrally-buoyant tracer particles are the most effective.[14]

2.3.2 *Birmingham Positron Camera*

The majority of work using PEPT has been by Dr. David Parker at the University of Birmingham using an in-house built positron camera. The camera, shown in Figure 7, consists of two large position sensitive detectors that can be rotated around the FOV to construct a 3D tomographic image.[5]

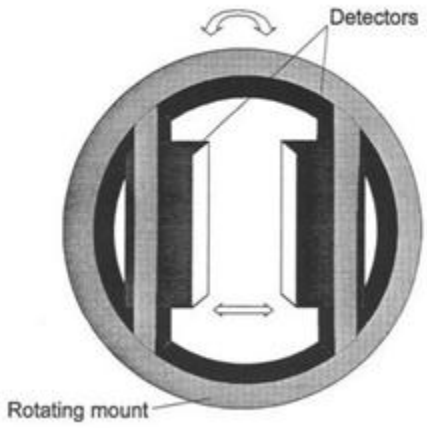

Figure 7: Schematic Diagram of the Birmingham Positron Camera[11]

The particle tracking capability is highly dependent on particle specific activity, which is dependent on particle size. Figures 8 and 9 show the activity distribution with particle size and the subsequent coincidence rates as a function of activity for a central F-18 source between two heads separated by 600 mm. A dead time model, R_m, was used to approximate the contribution of random

coincidences as $2\tau R_m^2$. Figure 9 shows the effect of these random coincidences with a dead time of 170 ns.[11] The limitation in count rate is partly due to the BGO crystals used in this older scanner detector heads, which requires a larger coincident window, and leads to larger dead time.

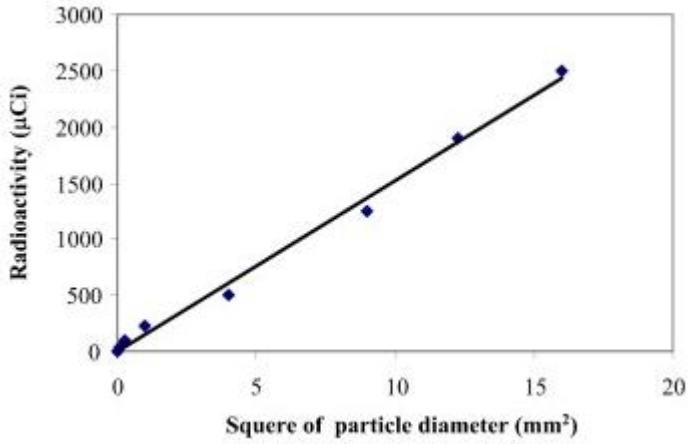

Figure 8: Effect of Particle Size on Achieved Radioactivity via Direct Activation[13]

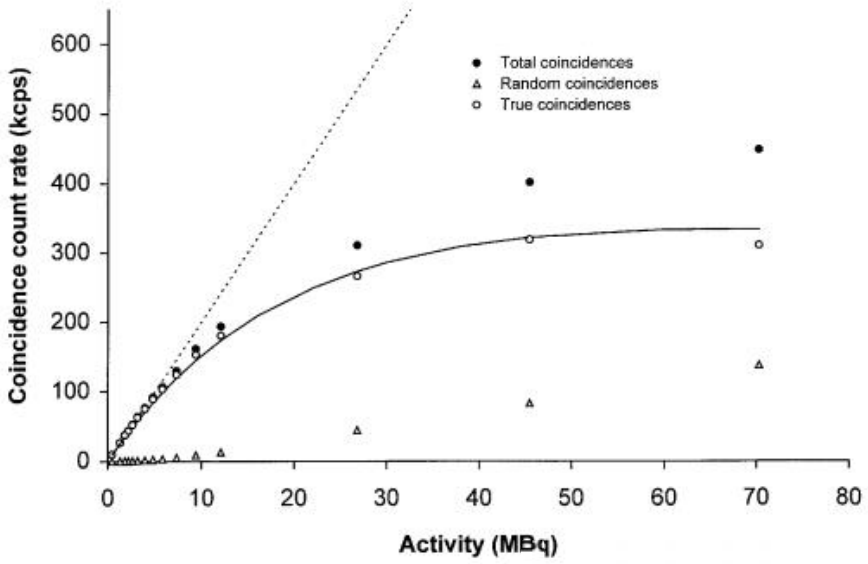

Figure 9: Photon Count Rate as a Function of Activity of F-18 Resin. The dotted line represents the dead time model $C_m = C_0(1 + R_0\delta)^{-2}$, δ=170ns. [11]

Parker et. al. are continually making improvement to the resolution and capabilities of their cameras. An F-18 tracer rotating in the xy plane at 1.4 m/s was located near 300 times per second with a r.m.s deviation of 0.6mm from the true location using their camera in 2002, as seen in Figure 10.[10]

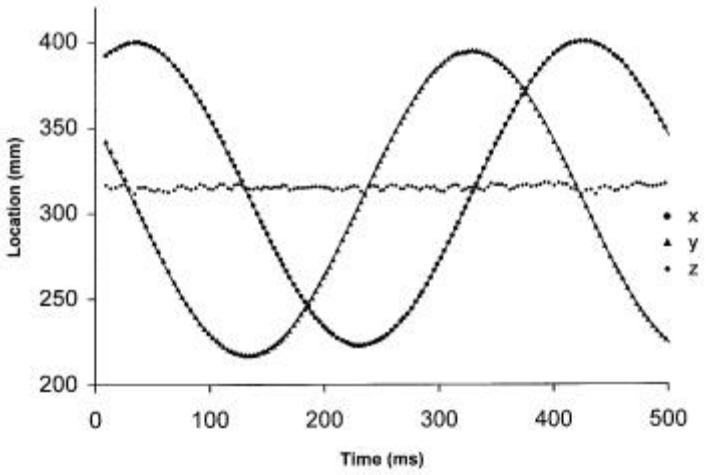

Figure 10: Tracked Particle Location Over Time for a F-18 Tracer Rotating in an XY Plane[11]

2.3.3 *PEPT Cape Town*

iThemba LABS in Cape Town, South Africa is the second operational PEPT facility in the world after Birmingham. Their ECAD 'EXACT3D' PET camera, shown in Figure 11, consists of 48 BGO detector rings and can achieve a transaxial FWHM spatial resolution of 4.8±0.2 mm and an axial spatial resolution of 5.6±0.5 mm.[15] This facility was established with considerable help from Dr. David Parker.[15]

Figure 11: Cape Town, South Africa's ECAD 'EXACT3D' PET Camera[15]

2.3.4 *PEPT Implementation in a Hydrocyclone*

A group in Bergen tagged resin beads with F-18 and injected them one at a time into a steady-state hydrocyclone flow at 10.55 meters per second.[16] A Siemens TruePoint PET scanner using LSO crystals allowing an energy window of 425-650 keV was used to track the particle inside the hydrocyclone. A coincidence timing window of 4.5 ns was deemed large enough to detect coincident gammas, but small enough to minimize detection of random gammas. The Bergen group mapped LORs to locate a point source within 200 microns within a fraction of a millisecond, as shown in Figure 12.

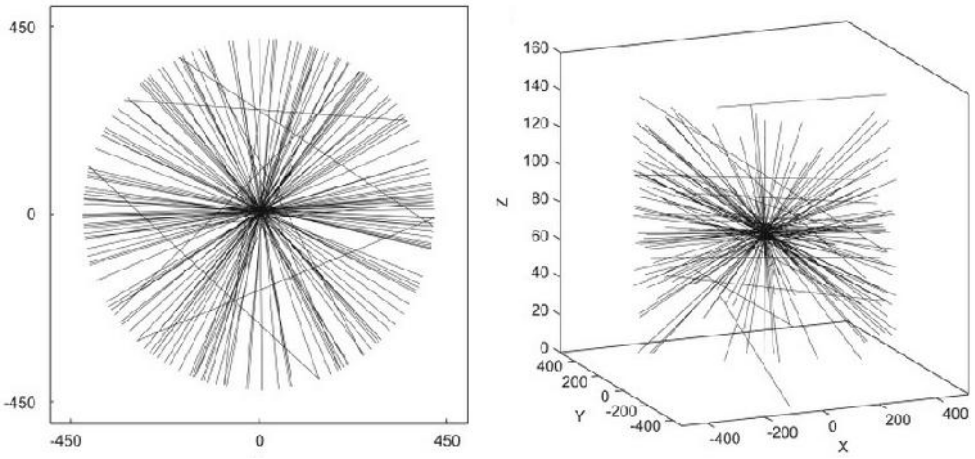

Figure 12: LORs Used to Determine Location of a Point Source[16]

Resolution in the x and y directions were less than 0.13 mm, and a bit higher in the z direction at 0.15-0.17 mm. The decrease in resolution in the z-direction is attributed to the limited angle subtended to the particle.[16] The group achieved a temporal resolution of 1 ms, but offered that increasing the frequency of timing words issued to the camera, currently limited to one every millisecond, would allow a temporal resolution down to 0.2 ms.[16]

2.3.5 *Other PEPT Applications*

PEPT is emerging for study a wide variety of engineering topics, and could be further extended to modeling multiphase flow. The technique has been used for studying solid-liquid mixing in drums, viscous fluid studies, fluidization and agglomeration, and to study flow pathways through saturated rock fractures.[11] A group in Canada is using PEPT for heavy particle flow studies in a spiral

concentrator[17] ,and particulate flow in a fluidized bed was studied by Schaafsma et al in the Netherlands.[18]

2.4 Particle Image Velocimetry

PIV uses a set of images to derive velocity vectors in the Eulerian description of the flow field. Acquiring PIV data requires four main components: (1) an optically transparent test section with flow that contains seeded particles, (2) a light source, such as a laser, (3) image recording hardware, and (4) software that can process the images into velocity fields.[19] Figure 13 illustrates a typical PIV experiment setup.

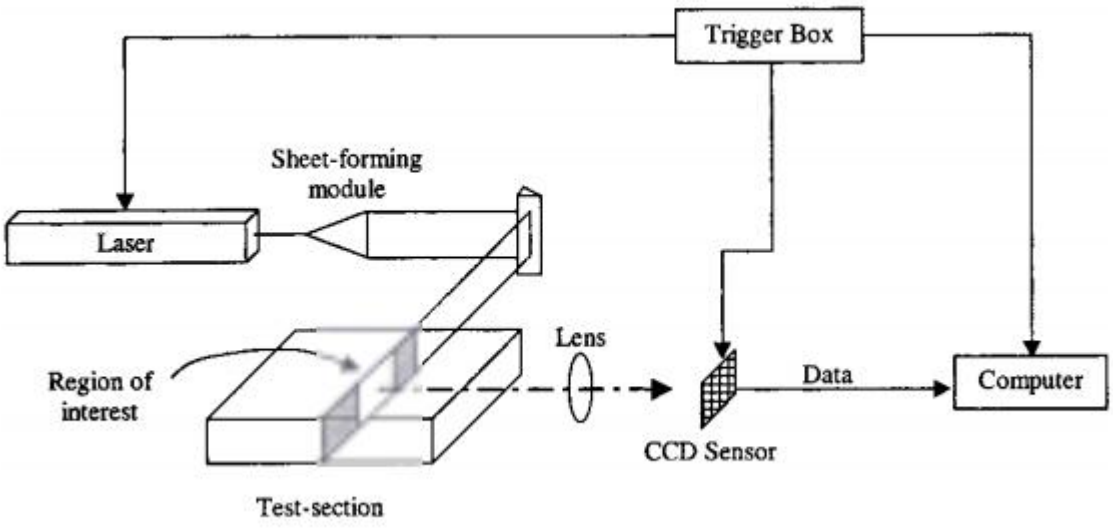

Figure 13: Diagram of a Typical PIV Setup[19]

2.4.1 *Seed Particles*

The seeded particles play an important role in PIV acquisition. They must follow the flow streamlines without excessive slip and efficiently scatter the illuminating laser light.[18] As long as the particle settling velocity is negligible in relation to the flow velocity, the first requirement will be fulfilled. The settling velocity, u_∞, is governed by the particle diameter, d_p, and density of the particles, ρ_p, as well as density and viscosity of the fluid, ρ_l and μ, respectively,

$$u_\infty = \frac{g d_p^2 (\rho_p - \rho_f)}{18\mu}.$$

Many accelerations may exist in the flow additional to gravity, g, and this criterion may be applied to them as well. It can be inferred from this equation that choosing a particle with small diameter and a density close to the density of the working fluid is optimal, especially in low velocity environments. Several sizes of plastic microspheres are available for PIV studies that have similar densities to water.

Such particles, however, also have a refractive index close to that of water causing them to scatter weakly in the laser light. Light scatter can be improved by increasing the particle size.

The concentration of seeder particles should produce more than 10 particle image pairs in each interrogation region in the gridded image field. while limiting the concentration so that it does not saturate the interrogation area.[20] More information on gridding of the image is provided in section 2.4.6.

2.4.2 *Laser and Optics*

A pulsed laser is normally used for PIV as it delivers the laser power to the interrogation area in short pulses as it creates a light sheet to illuminate the particles of interest. Pulsing allows for the camera to take two separate images: the first image is taken on the first laser pulse, and the second image on the second. The time between pulses allows for observation of the particle movement in between the pulses. The pulses are very short making manual camera timing nearly impossible. In most modern PIV experiments a synchronizer is employed to autonomously time the camera and laser pulses.[21] Figure 14 illustrates the timing relationship of the laser and camera. The longer camera exposure for the second laser pulse causes the second image of the particles to have a lighter background, as evident later in Figures 22 and 23.

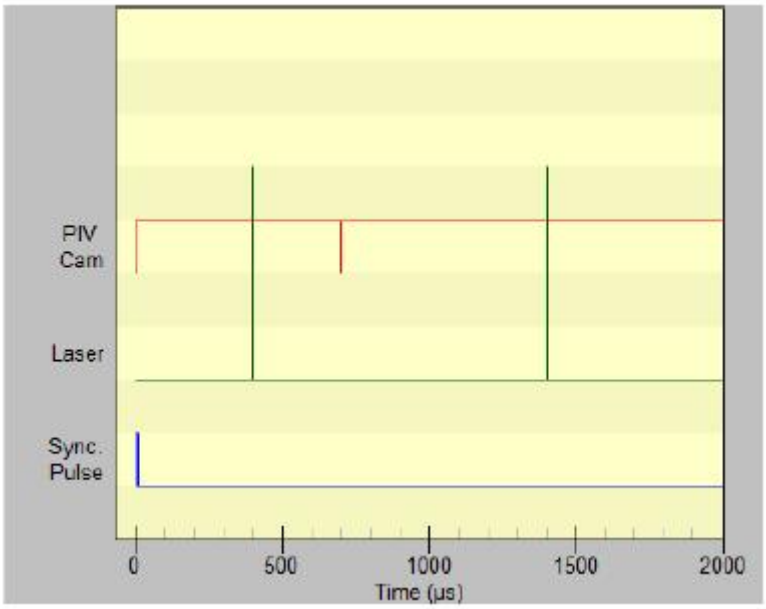

Figure 14: Laser-Camera Timing Diagram [2]

As the particles are illuminated by laser light, diffraction effects should be considered. Figure 15 depicts effects that that are governed by image magnification, *M*, focal length of the lens, *f*, image distance, d_i, object distance, d_o, and described in the following equations.[19]

$$d_o = (1 + M^{-1})f$$

$$d_i = (1 + M)f$$

$$M = {}^{d_i}/_{d_o}$$

The diameter of the lens aperture *D* and the laser wavelength λ contribute to consideration of the diffraction limited spot-size, d_s.

$$d_s = 2.44(1 + M)\frac{f}{D}\lambda$$

In combination with the f-number of the lens the effective particle image diameter can be described as follows.

$$d_e = (M^2 d_p^2 + d_s^2)^{1/2}$$

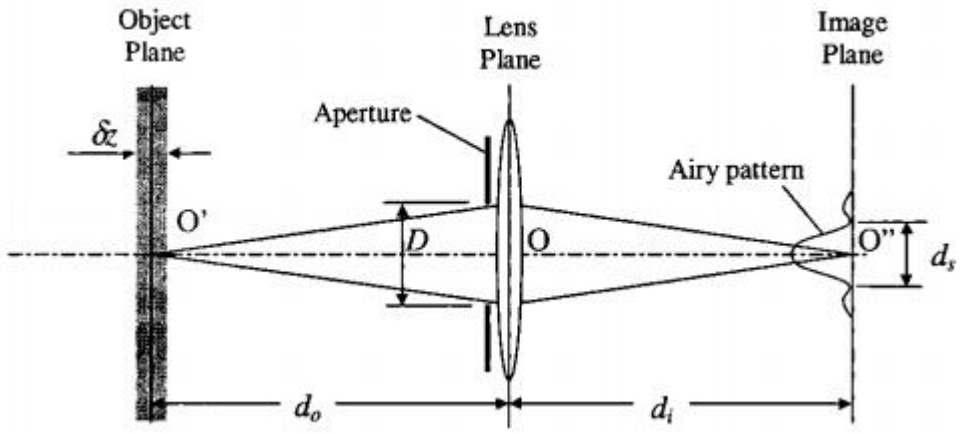

Figure 15: Diffraction Effects During Particle Image Recording.[19]

It is important to avoid imaging particles that are out of focus in the interrogation area. The depth-of-field, δz , must be thinner than the light sheet thickness in order to ensure all particles are in focus.

$$\delta z = 4(1 + M^{-1})^2 (\frac{f}{D})^2 \lambda$$

2.4.3 *Laser Safety*

The class of a laser characterizes the power and wavelength of a laser. The higher the class of laser, Class I-Class IV, the more hazardous it is. The most likely laser injury is one to the eye or skin. The low divergence angle and coherence of a laser in combination with the focusing ability of the lens of an eye can lead to laser radiation being concentrated on a small area of the retina, even very short exposures can destroy parts of the retina. Eye injuries happen in fractions of a second and goggles made specifically for protection against

relevant wavelengths should be worn at all times when a laser is on, even if the laser is not firing. To protect your skin from burns you should not position any body parts in the line of the laser.

2.4.4 *Recording Device*

Charge-coupled devices (CCD) sensors are most often used to record images. While they may be a bit limiting in resolution, they are exceptionally sensitive to light, allowing for use of a less powerful laser, which is not only more cost effective, but also safer.[19]

In older PIV methods the film transport inside the camera and digitalisation with the film scanner lead to uncertainties in particle location between each image. Measuring an artifact consistent in each image was used to control this uncertainty and guarantee a reliable PIV investigation.[19]

2.4.5 *Errors Associated With PIV*

Tracking error occurs when the particles slip relative to the flow. Random error can be introduced through noise or inaccurate particle correlations being made between the image sets, and typically goes with the effective image diameter as

$$\sigma_{random} = cd_e$$

with c varying between 0.05 and 0.10 depending on experimental conditions.[19]

Bias error originates during processing when trying to calculate particle

displacement to sub-pixel accuracy. The correlation field is typically 32 x 32 pixels, so when using a curve-fit or centroiding scheme to determine the sub-pixel location, bias and random errors arise. Practitioners suggest maintaining an effective particle image diameter of approximately two pixels to minimize the balance between bias and random error.[19]

The rotation and deformation experienced in turbulent flow incites a gradient error that leads to a loss of correlation, and lastly there is an unavoidable acceleration error. The acceleration error stems from the inherent nature of PIV which uses a Lagrangian frame of reference, i.e. the particle, to approximate an Eulerian flow velocity.[19]

2.4.6 *Processing of PIV Images*

A 32 x 32 grid will result in a 32 x 32 array of independent velocity vectors. In reality, the vectors are often not independent as there may be up to 50 % overlap in both x and y directions, based on user settings. Bad vectors, or spurious vectors, are vectors that are significantly different from their neighbors and may be caused by some sort of noise. If a bad vector is calculated it can be replaced with a vector value based on the average of the neighbor cells. Prediction of mean velocities can be accurate with very few PIV images, but many more are needed for a production of turbulence statistics.[21,22]

2.4.7 *PIV Rules of Thumb*

Keane and Adrian's five rules of thumb for PIV analysis combined with the TSI's commercial software package for image processing to provide a list of rules to follow for optimal PIV results. Rule 1 recommends the interrogation spot size be small enough that the flow inside is described adequately by a single vector. Rules 2 and 3 require more than ten particle image pairs per interrogation spot, and maximum displacements of these pairs should be less than 1/4 of the spot size, respectively. Rule 4 states the maximum displacement outside of the plane displacement should not exceed 1/4 of the light sheet thickness, and Rule 5 recommends the minimum in-plane displacement should be two particle image diameters. [20] TSI adds that exposure must be long enough to clearly depict the particles.[4]

2.5 Relationship of Lagrangian and Eulerian Velocities

In a Eulerian frame of reference, velocities are gleaned from investigating a specific area in the flow and monitoring particles moving through the area over time. Quantitatively the flow is a function of location in the interrogation window (x) and time (t).

Conversely, in a Lagrangian frame of reference an individual particle is followed over time, and the trajectory is described as a function of position a, and time t. The Eulerian and Lagrangian specifications are related by the equation

$v(X(a,t),t) = \frac{\partial X}{\partial t}(a,t)$. X and a are referred to as the Eulerian and Lagrangian coordinates.

The Eulerian representation of PIV velocities must be related to the Lagrangian representation of PEPT velocities for a validation to be possible. While Eulerian flow fields are convenient to measure, Lagrangian flow models occur naturally in turbulent diffusion theories.[23] The transformation of Lagrangian data into an Eulerian frame of reference requires statistical approximations that are most found in atmospheric and oceanic studies.

2.5.1 *Turbulent Advection-Diffusion*

The seeded particles in the flow loop are subjected to advection and diffusion transport upon entering the test section. Advection describes the movement of the particles from one area in the flow to another, caused by the bulk motion of the fluid. The diffusion of particles is characterized as particle movement through the fluid independent of time average fluid motion. Partial differential equations (PDE) derived from the mass conservation equation describe the advection and diffusion processes. Advection is described as[27]:

$$\frac{\partial}{\partial t}u(x,t) + \frac{\partial}{\partial x}\big(a(x,t)u(x,t)\big) = 0$$

The diffusion process is random, and for steady-state environments, the flux, ***J***, in atoms/(m^2-s) describes the number of particles passing through a unit area per unit time. The lateral, y, diffusion is controlled by the one-dimensional representation of Fick's First Law of Diffusion[28]:

$$J = -D\frac{dC}{dx}$$

D is the diffusion coefficient in m^2/s and dC/dx is the concentration gradient of particles in the fluid in atoms/m^4. If a stream of concentration C_0 is injected into a main flow at position z_0, then the concentration profile downstream is controlled by the combined actions of advection and diffusion. The diffusion time is governed by the time the fluid element has traveled in the flow from the injection point as $t = \frac{x}{\bar{u}}$. This kind of flow was studied earlier using PET imaging.[27] Perfect particles will follow fluid molecules exactly, such that the concentration of a series at a point in the flow is proportional to the probability of a particle trace passing through that same point in the flow. Figure 16 demonstrates particle motion subject to advection-diffusion.

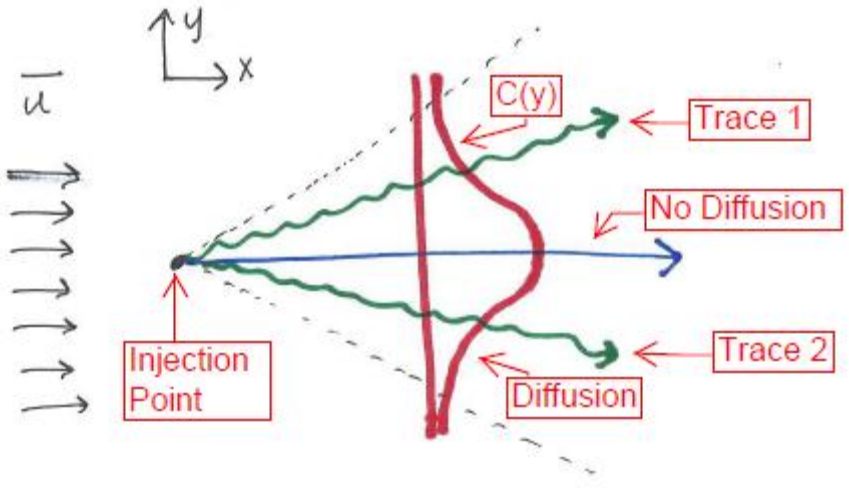

Figure 16: Advection-Diffusion of a Particle Downstream of Injection Site.

In a non-steady-state environment, Fick's Second Law of Diffusion offers a description in the rate of change in the concentration over time[28]:

$$\frac{dC_x}{dt} = \frac{d}{dx}\left(D\frac{dC_x}{dx}\right)$$

Concentration downstream of a source is consistent with planned experiments, and is represented as [28] :

$$\frac{\partial C}{\partial t} = D\nabla^2 C - \vec{u}\cdot\nabla C$$

At steady state:

$$\frac{\partial C}{\partial t} = 0.$$

The concentration at z_0 is governed by particle injection rate and test section geometry.

Turbulent flow conditions cause the diffusion in the flow to be dominated by the turbulent diffusivity. The kinetic energy in the flow creates eddies that break in to smaller eddies and dissipate via viscous dissipation.[27] Turbulent velocity fluctuations vary with time and are random, and will convert particles along trajectories in the flow that continuously vary in time and space.

2.5.2 *Independence Approximation and Power Spectrums*

S. Corrsin[23] postulated that a rough estimate of the Lagrangian flow in terms of Eulerian data can be derived from basic turbulence theory. In one dimension, the Lagrangian velocity describing a particle position x(t) is $u_L(t) = \frac{dx}{dt}$, and is related to Eulerian velocities by $u_L(t) = u_E(x(t), t)$. This description

indicates that a Lagrangian velocity at time t is the Eulerian velocity measured at x(t).[23] Corrison suggested an *independence approximation* to relate the Lagrangian and Eulerian correlation functions, R_L *and* R_E respectively when $\tau_c k_0 u^* \ll 1$. τ_c is the Lagrangian e-folding time, k_0 is the characteristic wavenumber of the turbulence, and u^* is an effective velocity in terms of a two-point ternary correlation function.[22] When the independence approximation is valid, $R_L \ll R_E$. The Eulerian correlation function is as follows:

$$R_E(r - r_0, t) = \langle u'(r, 0)u'(r_0, t)\rangle$$

where u(r,t) is the fluid velocity at position r and time t, and u' is the fluctuating part of u. $\bar{u}$ is the mean flow velocity of the fluid. It can then be derived that the Lagrangian correlation function is

$$R_L(t) = \langle u'(r, 0)u'[x(r, t), t]\rangle.$$

With a constant mean velocity $x(r, t) = r + t\bar{u} + \int_0^t dt' u'[x(r, t'), t']$.

Assuming the particle displacements are much less than the size of the system and the variable velocities are statistically independent of the dirac delta function, the Lagrangian correlation function can be related to the Eulerian as Corrsin's independence approximation.

$$R_L(t) \approx \int dr_0 \langle u'(r, 0)u'(r_0, t)\rangle\langle\delta[x(r, t) - r_0]\rangle$$

To assess the validity of the independence approximation, the Lagrangian correlation equation is divided into an independent approximation term and a correction term.[23]

A relation of Lagrangian and Eulerian data can also be approached as a comparison of energy spectrums. From Andrey Kolmogorov's inertial subrange theory, an Eulerian three-dimensional turbulent energy spectrum can be described by a time rate of turbulent kinetic energy dissipation per unit mass, ϵ, turbulence wave number, *k,* and a dimensionless constant, *N*, as follows.

$$\mathcal{E}(k) = N\epsilon^{2/3}k^{-5/3}.$$

Application of this equation to an expression for turbulent energy gives a rough estimate of the Eulerian turbulent integral scale.[23]

$$\frac{1}{2}\overline{u^2} = \int_0^\infty \mathcal{E}(k)dk$$

When Reynolds numbers are large, considering k^* is Kolmogorov's wave number and k_0 is the characteristic wave number of energy-bearing eddies, the integrand can be approximated as

$$\mathcal{E}(k) = \begin{Bmatrix} 0 & for & k < k_0 \\ N\epsilon^{\frac{2}{3}}k^{-\frac{5}{3}} & for & k_0 \le k \le k^* \\ 0 & for & k > k^* \end{Bmatrix}.$$

For similar Reynolds numbers the Lagrangian spectrum can be approximated in a similar fashion, considering Kolmogorov's frequency, w^* and the energy-bearing part of the Lagrangian spectrum, w_L.

$$\phi_{11}(w) = \begin{Bmatrix} 0 & for & w < w_L \\ B\epsilon w^{-2} & for & w_L \le w \le w^* \\ 0 & for & w > w^* \end{Bmatrix}$$

When fluid density is constant, and the turbulent environment is homogenous and stationary, the Lagrangian and Eulerian mean square velocities are equal and

$$\overline{v_1^2} = \overline{w_1^2} \approx B\epsilon w_L^{-1}$$

Time correlation between Eulerian and Lagrangian spectrums is derived in a nearly identical manner, but considering a constant other than B. There are no real estimates of these constants, but they are hoped to be unity.[23]

Wandel and Hansen integrate Kolmogorov's and Corrson's theories with statistical theory of shot effect noise and Helmholtz theorems to derive analogous Lagrangian and Eulerian power spectrums as transforms of their energy spectrums characteristic of their kernel functions.[25]

$$P_L(w) \cong \frac{\sqrt{\pi}}{4}\frac{1}{u'}\mathcal{E}\left(\frac{\sqrt{\pi}}{4}\frac{w}{u'}\right)$$

$$P_E(w) = \int_0^\infty dk\mathcal{E}(k)\left[K_E\left(\frac{w}{vk}, \frac{v}{\sqrt{2}u'}\right)/u'k\right]$$

Lagrangian and Eulerian kernel characteristics are described in Figure 17.[25]

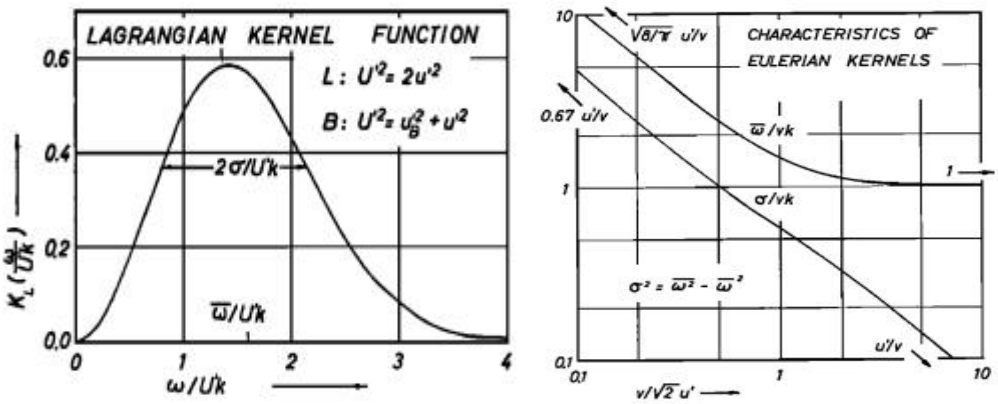

Figure 17: Lagrangian and Eulerian Kernel Function Characteristics.[25]

CHAPTER 3

1ST PIV EXPERIMENT

3.1 PROJECT DEVELOPMENT

An experiment is designed to support both PIV and PEPT flow measurement. The PIV measurements are provided herein, as are plans for the PEPT experiments to follow.

3.1.1 *Test Section Construction*

The initial test section was a narrow duct designed to accommodate a turbulent water flow suitable for both PIV and PEPT investigation. Design constraints included a test section that could fit inside an 8" diameter scanner bore, a turbulent flow, and a velocity of less than 1 meter per second. A slow velocity was necessary to maintain tracer position resolution during the PEPT experiment. Knowing the pump would provide roughly 7 gallons per minute from a 1" pipe, a velocity was calculated in the following manner:

$$6.8\frac{gal}{min} \times \left[\frac{1\,min}{60\,s}\right] \times \left[\frac{1\,m^3}{264.172\,gal}\right] \times \left[\frac{1}{A_{xs}}\right] \leq 1\frac{m}{s}$$

This implies the test section's cross-sectional area must be greater than 0.00043 meters. Choosing a Reynolds number maximum of 10,000, another cross-section limit can be determined assuming a kinematic viscosity of water of $1.004 \times 10^{-6}\frac{m^2}{s}$.

$$Re \geq \frac{Ud_h}{\upsilon} \rightarrow d_h \leq \frac{(10{,}000)(1.004 \times 10^{-6}\frac{m^2}{s})}{1\frac{m}{s}} = 0.01004\,m$$

This gives an upper limit for the hydraulic diameter and the cross-sectional area limit can be further deduced.

$$d_h = 0.01004\,m \leq \frac{4A_{xs}}{P_w} = \frac{4(W)(H)}{2(W+H)}$$

The test section must also fit in an 8" preclinical PET scanner bore. Considering these limitations, a width of 2.5" and height of 0.5" were chosen, with the rubber gasket adding 0.25" to the height. The resulting cross-sectional area was 1.875" yielding a hydraulic diameter of 2.308" or 0.0586 meters.

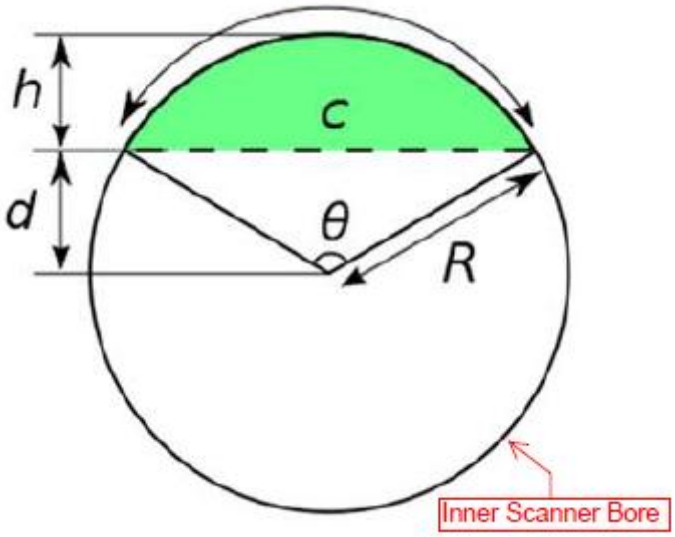

Figure 18: Method of Deriving Maximum Limit of Hydraulic Diameter

1/2" thick material was selected increasing the total outer cross section to 3" x 1.25". Using the width and bore radius, and assuming the test section is guided into the center of the bore, where sensitivity is maximum, the maximum test section width that can penetrate the scanner bore is given as;

$$\theta = 2\cos\left(\frac{h}{2R}\right) = 1.98\,radians$$

$$c = 2R\sin\left(\frac{\theta}{2}\right) = 6.68"$$

in which the parameters correspond to Figure 18.

6.68" is more than the tentative width of 3", so the test section will fit in the bore. With these dimensions, an estimation of the velocity inside the test section can be made based on measured flows from the 1" pipe.

$$(\rho U A_{xs})_{pipe} = (\rho U A_{xs})_{ts} \rightarrow U_{ts} = \frac{(UA_{xs})_{pipe}}{(A_{xs})_{ts}} = \frac{(0.38)(0.0005)}{0.0011} = 0.175 \frac{m}{s}$$

However, the measured velocity, using PIV, was actually closer to 0.38. This is probably due to fouling in the turbine flow meter that was used to measure flow rate in the pipe. A test will be done to recalibrate by emptying flow into a two gallon bucket to measure the time it takes to fill. A Reynolds number of 22,179 exists in the test section based on the PIV measured velocity and viscosity of water at 20°C.

$$Re = \frac{(0.38)(0.0586)}{1.004 \times 10^{-6}} = 22{,}179$$

A drawing of the proposed test section was made in AutoCAD, seen in Figure 19. Several slabs of 1/2" thick acrylic were chosen for optical clarity, as is necessary for PIV measurements. A table saw cut the slab to two 28" x 3.5" pieces for the top and bottom. Two 3.5" x 0.5" pieces were also fabricated that made up the ends, and two 27" x 0.5" pieces were fabricated for the sides of the test section. A drill press was used to drill an inlet and outlet hole in the top and bottom pieces. A second, much smaller hole was drilled and tapped in the top piece to accommodate a fitting for future particle injection. PVC adapters were glued to the inlet and outlet to be connected to the loop tubing.

The bottom, sides, and end pieces were glued together with acrylic glue, and then a piece of rubber gasket was glued to the top of the full bottom piece, to create a 27" x 2.5" x 0.75" flow channel. It would have been beneficial to leave the protective paper on the acrylic until all the gluing was done to avoid scratches

from having to remove the excess glue. A piece of nylon mesh was attached inside the test section just below the inlet to straighten the flow. 16 spring clamps sealed the top piece to the rest of the test section as shown in Figure 20**.**

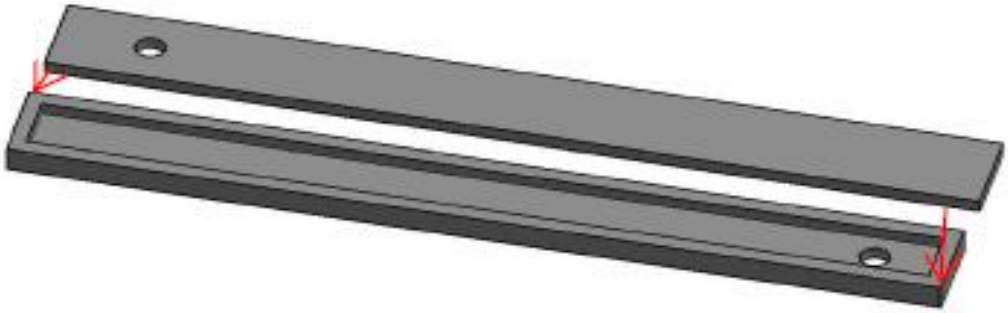

Figure 19: AutoCAD Drawing of Proposed Test Section.

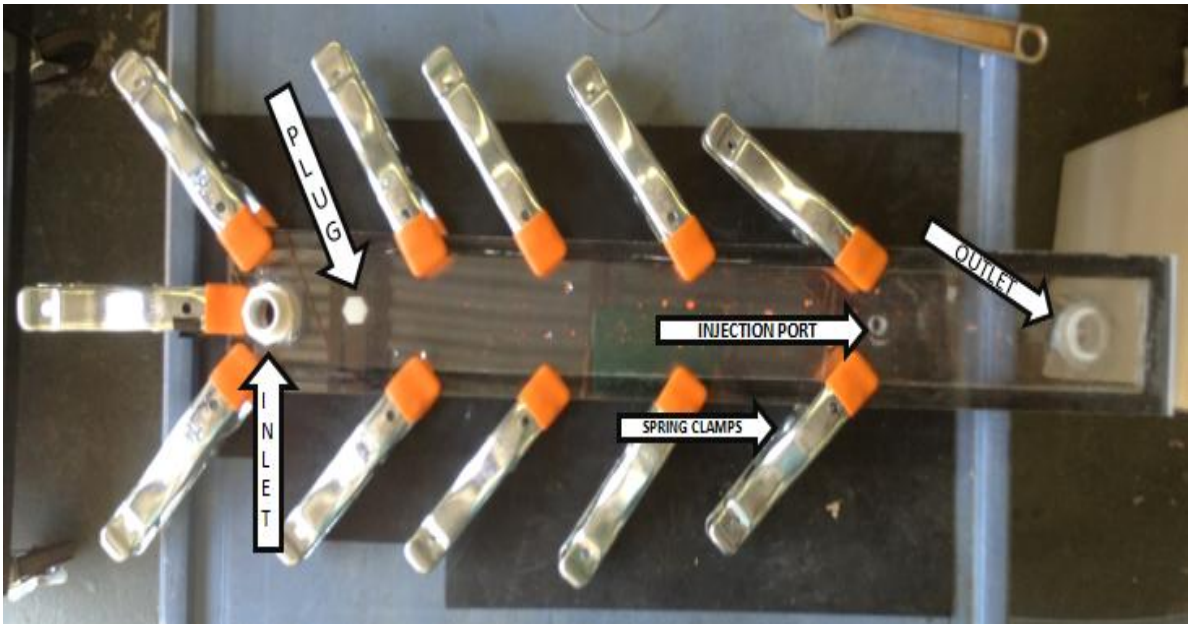

Figure 20: Constructed Test Section.

3.1.2 *Flow Loop Construction*

The flow loop for the PIV experiment is portable to allow transport to the UT Hospital for subsequent testing using the preclinical scanner. The flow loop is comprised of a header tank supplying a 3MD LittleGiant pump that leads to a flow meter and the first length of MasterKleer PVC tubing connected to the test section inlet. More PVC tubing connected to the outlet leads to a PVC tee. One leg of the tee leads to the exhaust tank, while the other allows a PVC tube to recirculate back to the header tank. A plug is inserted into the hole intended for activated particle injection. A capillary tube will be fitted to the hole and connected to a syringe for activated particle insertion during the PEPT experiments. A NanoJet syringe pump was used to remotely inject the F-18 into the test section in prior imaging of advective diffusion flows using PET.[27] However, current plans for the PEPT tests have the particles manually injected using a shielded syringe. Figure 21 shows the flow loop setup.

Figure 21: Test Section and Flow Loop Setup.

3.2 Experimental Conditions

A Class IV laser is setup on its side parallel to the side of the test section. Protective goggles were worn at all times when the laser was on. A metal arm suspends the camera and lens above the test section perpendicular to where the laser light will illuminate the seeded particles. Table 2 lists the acquisition equipment used in the PIV experiment.

Table 2: Equipment List for PIV Experiment

Component	Model/Version
Capture/Processing Software:	Insight 4G V.10.0.3.22
Camera:	Powerview Plus 4MP
Capture Card:	Xcelera-CL PX4
Capture Card Software/Driver:	Teledyne DALSA Cam-Expert V.7.10.00.1022
Laser:	YAG New Solo I
Synchronizer:	LaserPulse Model 610036

Below in Table 3, the PIV experimental conditions are listed. A flow meter was used to measure the velocity of the water leaving the pump before it entered the test section. This velocity was recorded after the loop had been running for 5 minutes to acquire steady state conditions. The fluid temperature was measured using a thermocouple inside the header tank.

Table 3: Experimental Conditions

Fluid:	Water
Fluid Temperature:	20°C
Channel Geometry:	Rectangular Duct
Channel Length:	26.5"
Channel Width:	2.3125"
Channel Height:	0.75"
Flow Rate in Turbine Meter:	0.38 m/s
Reynold's Number:	22,179

The seeding particles in Table 4 were chosen with a density equal to water to maintain a negligible settling velocity.[19]

Table 4: Experimental Parameters

	Seeding Properties	
	Seeding Particle	1.00 g/cc polyethylene spheres
	Particle Size	106-125 µm
	Seeding Concentration	3.1g/23kg H20
	Camera/Lens Properties	
	Camera Resolution (Square)	2048 Pixels
	Lens	AF Nikkor 40 mm
	Focal Length Setting	40 mm
	Relative Aperture	14.3
	Area of Interest	250x250 mm
	Laser Properties	
	Laser Speed	15 Hz
	Wavelength	532 nm
	Energy	15 mJ
	Energy Stability	±4%

The time of the pulse separation for a series of images, shown in Table 5, was chosen to maximize resolution. If the time is too long, acceleration error can dominate the data. Conversely, if the time is too short, particle movement may be indistinguishable from random error. An excel file provided by LaVision was used to determine the most efficient pulse separation.

Table 5: Timing Parameters

Timing Parameters	
Desired Pixel Displacement	6.4 mm
Expected Avg. Velocity	0.38 m/s
Pulse Separation (Δt)	1500 μs

Water was pumped through the test section from the header tank at approximately 6.8 gallons per minute through the flow meter, creating a mean flow velocity of approximately 0.38 meters per second in the test section. These initial tests use relatively slow flow velocities to limit particle specific activities required for the PEPT experiments while maintaining a turbulent environment.

3.1 grams of 106-125 micrometer diameter polyethylene Cospheric© microspheres were mixed initially with a soapy water solution, and then poured into the header tank. This procedure discourages agglomeration of particles in the flow. A series of 500 images were taken in an interrogation area 13" from the inlet to 17" from the inlet. A single set of images is shown below in Figure 22 and Figure 23, demonstrating the visible movement of the particles.

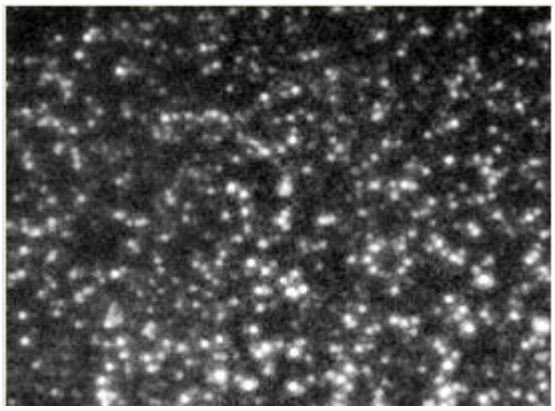

Figure 22: First of a Set of Pictures of Particles in the Interrogation Area of the Test Section.

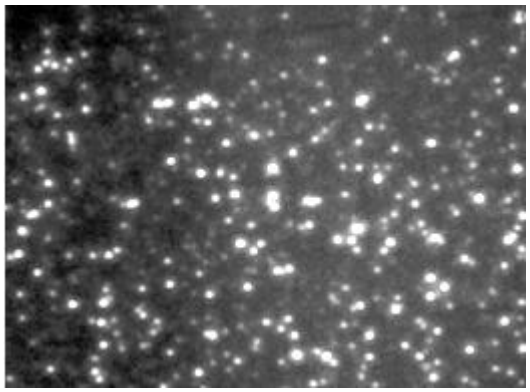

Figure 23: Second of a Set of Pictures of Particles in the Interrogation Area of the Test Section.

After the images were taken, a local validation post processor within Insight was applied during the data processing stage. In the case of a spurious vector, the vector would be replaced with the local 5x5 median velocity. Upon completion of the image processing, *Tecplot* was used to develop plots for data analysis

3.3 Results

There are 197.8 micrometers per pixel. Using 32 x 32 pixels, a velocity vector should appear roughly every 6.4 mm. Figure 24 shows the averaged instantaneous velocity vectors.

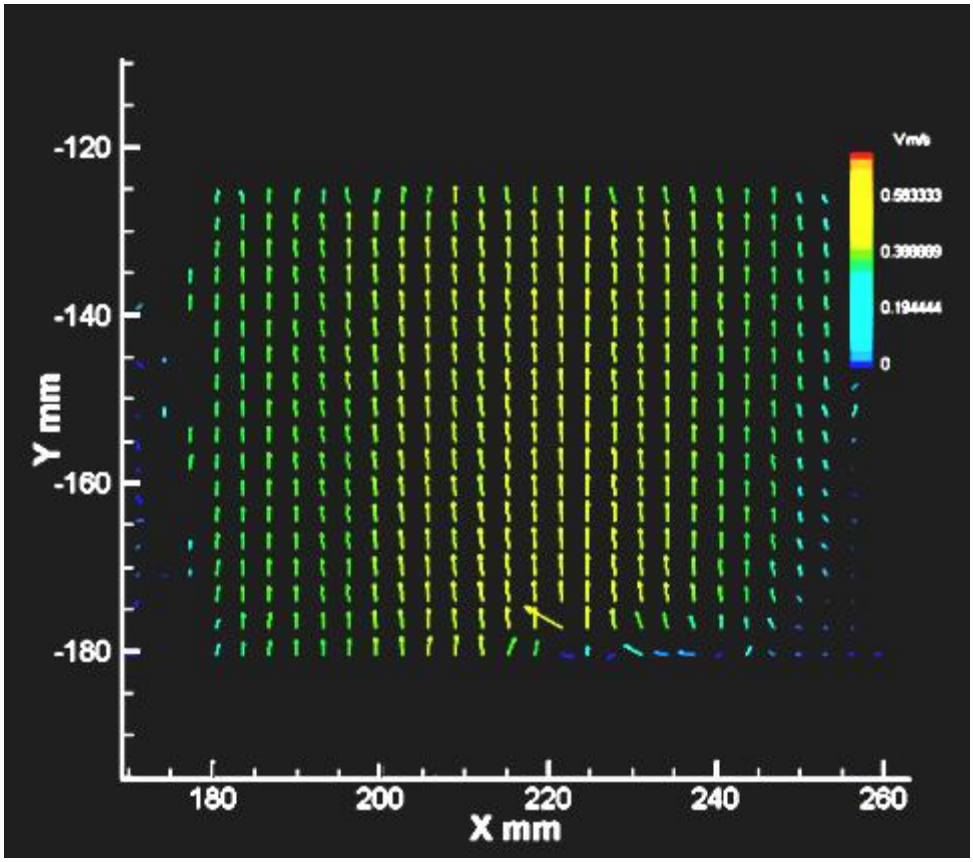

Figure 24: Vector Plot of Interrogation Area

Figure 25 is a velocity profile contour map of the interrogation area of the test section. The dark blue color in the bottom right corner represents zero velocity. The zero velocity region is attributed to the camera lens not always

accurately distinguishing the particles on the edge of the image because not enough light reaches that region of the flow. This causes Tecplot to not accurately represent the particle movement.

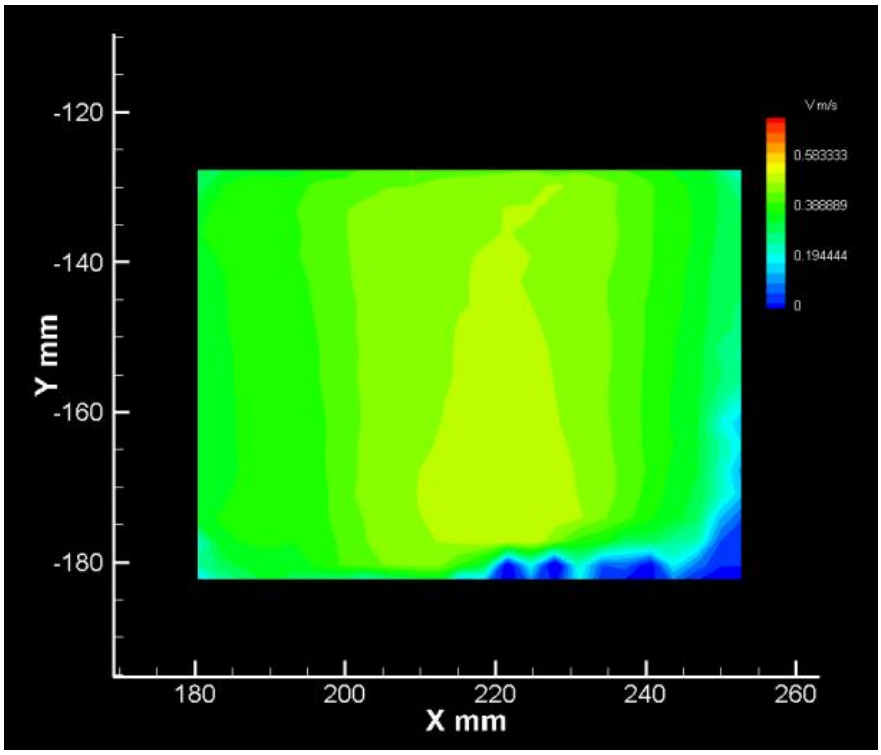

Figure 25: Contour Map of Velocity Profile

Figure 26 is a graphical representation of the velocity profile across 10 separate slices of the interrogation area from x=180mm to x=248mm. Each slice is approximately five millimeters farther downstream than the slice before it. As can be observed, the flow is pulling to the right as was evident during the experiment. Vortical flow at the outlet, a few more inches downstream of these measurement cross-sections, is causing a distortion of the upstream flow profile.

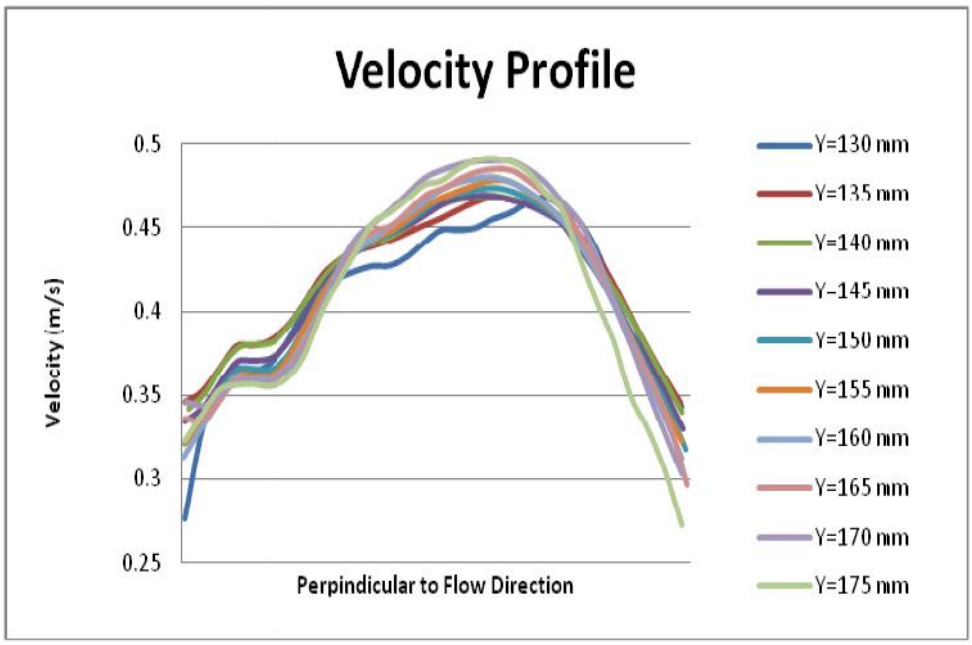

Figure 26: Velocity Profile of 10 Consecutive Downstream Locations.

Calculating the mean velocity <u> as

$$< u > = \frac{1}{N}\sum_{i=1}^{N} x_i \ ,$$

the standard deviation σ_v of these velocities is 0.051686 with

$$\sigma_u = \sqrt{\frac{1}{N-1}\sum_{i=1}^{N}(x_i - < x >)^2}$$

Gradient and acceleration errors must be considered when investigating turbulent flow. Rotation and deformation prevalent in turbulent flows will lead to a loss of correlation within the interrogation window. While gradient error is probable, acceleration error is unavoidable when using a Lagrangian motion of

particles to approximate Eulerian instantaneous velocities. Acceleration error is mathematically described as

$$acc = \frac{\overline{v_1} - \overline{v_2}}{\Delta t}$$

and is illustrated in Figure 27.[19]

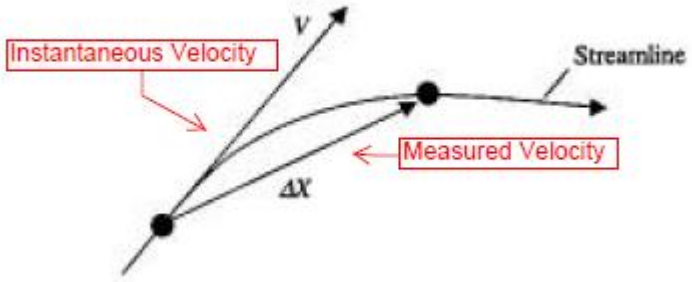

Figure 27: Acceleration Error in Eulerian Approximation of a Particle Using Lagrangian Particle Displacement.[19]

In this PIV experiment a 15 Hz laser was used, so an image pair could only be acquired every 1/15 seconds. The spatial resolution is limited by the four megapixels in the camera, the particle size, and the field of view.

CHAPTER 4

2ND PIV EXPERIMENT

4.1 TEST SECTION IMPROVEMENT

In order to improve the PIV data for the purpose of validating PEPT as a particle tracking method, another set of images will be taken with some adjustments. A similarly sized, improved test section, shown in Figure 28 and Figure 29, accommodates a sealing system of nylon bolts rather than metal clamps. This further minimizes potential water leaks and simultaneously improves the structure for the PEPT experiment. The first test section uses metal clamps, and metal near the PET scanner scatters gammas and creates image artifacts.

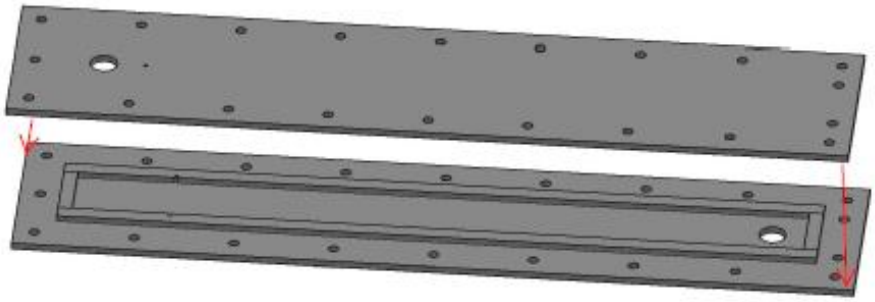

Figure 28: CAD Drawing of Improved Test Section.

Figure 29: Improved Test Section

The bolt sealing technique widened the test section, so the flow cross section was decreased to ensure the test section still fits in the scanner bore. The new flow cross section is 2.3125" x 0.75".This estimates a new d_h of 1.13", and a corresponding Re of 10,888. The particle size will also be reduced to 53-60 micrometers to improve spatial resolution.

CHAPTER 5

FUTURE PEPT EXPERIMENT

5.1 PROJECT DEVELOPMENT

The UT Medical Center provides a Concord Micro Systems MicroPet P4 Scanner for the initial PEPT experiment. Figure 30 depicts the scanner and Table 6 gives a list of scanner specifications. The test section described in Chapter 4 will remain stationary inside the scanner bore while 400-600 micrometer resin beads activated with near 2 uCi of F-18 are injected into the flow. A thin piece of acrylic tube is inserted into the bore around the test section to mitigate water damage to the scanner should a leak occur.

Software is currently being developed to convert the list mode output from the scanner to lines of response (LOR) to be used for particle tracking analysis.

5.1.1 *PET Scanner*

Table 6: Scanner Specifications[26]

MicroPet P4 Specifications	
Port Diameter	22 cm
Axial FOV	8 cm
Timing Window	2,6,10,14, or 18 nsec
Energy Window	0-810 keV
Absolute System Sensitivity	2.25%
Reconstructed Volumetric Resolution	6.4 uL

Figure 30: Siemens P4 Scanner[26]

5.1.2 *Protocol*

A protocol was written to prepare for the first trip to the hospital, and submitted to the radiation safety committee at the University of Tennessee. When handling radiation, preparedness and knowledge of possible accidents is essential to conducting a safe experiment. A protocol provides a step by step description of the experiment; this not only reduces potential error during the

experiment, but the process of forming the protocol can help to identify weakness in the process. The protocol written and approved by the Radiation Safety Department for the PEPT experiment follows:

Approved Protocol

PROLOGUE:

The following is the proposed method for obtaining Positron Emission Tomography (PET) scans of F-18 activated particles traveling through a water loop. The water loop has already been tested and monitored on several occasions with particles in the flow for optical measurement using a Particle Image Velocimetry (PIV). This protocol is for collecting similar data using activated particles in a PET scanner. The loop must be transported to the hospital in sections and constructed around the PET scanner. The method for construction, maintenance, and deconstruction of the loop, as well as the injection of the activated particles is described herein. The actual activation of the particles is addressed in the accompanying protocol "Ion Column Resin Bean F18 Activation Procedure", supplied by Brian Hall. The text in red describes the part of the activity when someone will be getting some exposure to F18 gammas while loading a syringe into a syringe pump.

BEFORE TRANSPORT TO UT HOSPITAL:

1. Wax the inside of the bottom, sides, and top of the test section. This reduces particle adhesion to test section surfaces.
2. Secure top of the test section. Place one spring clamp on the end of the test section closest to the inlet, and a clamp on each adjacent corner at a 45 degree angle. Put a clamp on each side of the test section at a 45 degree angle at 4, 8, 12, and 16 inches from the end. The rubber tips of the clamps should be positioned over the rubber gasket. Make sure there are 5 clamps left to take to the hospital.
3. Secure relevant fittings into the injection ports

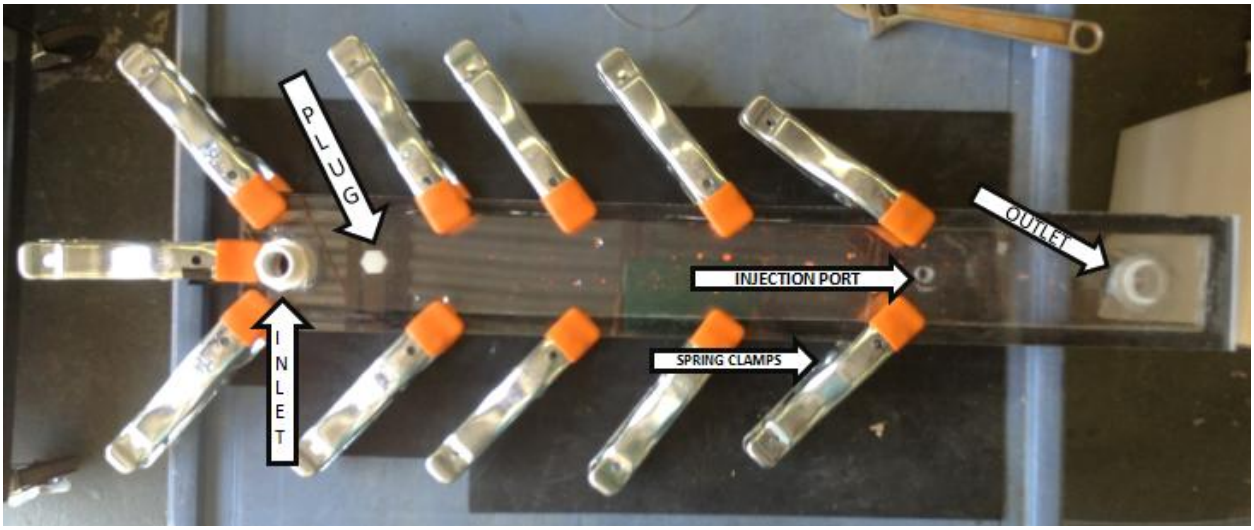

Figure 31: Test Section

4. Check the materials list to make sure all necessary materials are in the cart for the experiment.

AT THE HOSPITAL:

Setup:

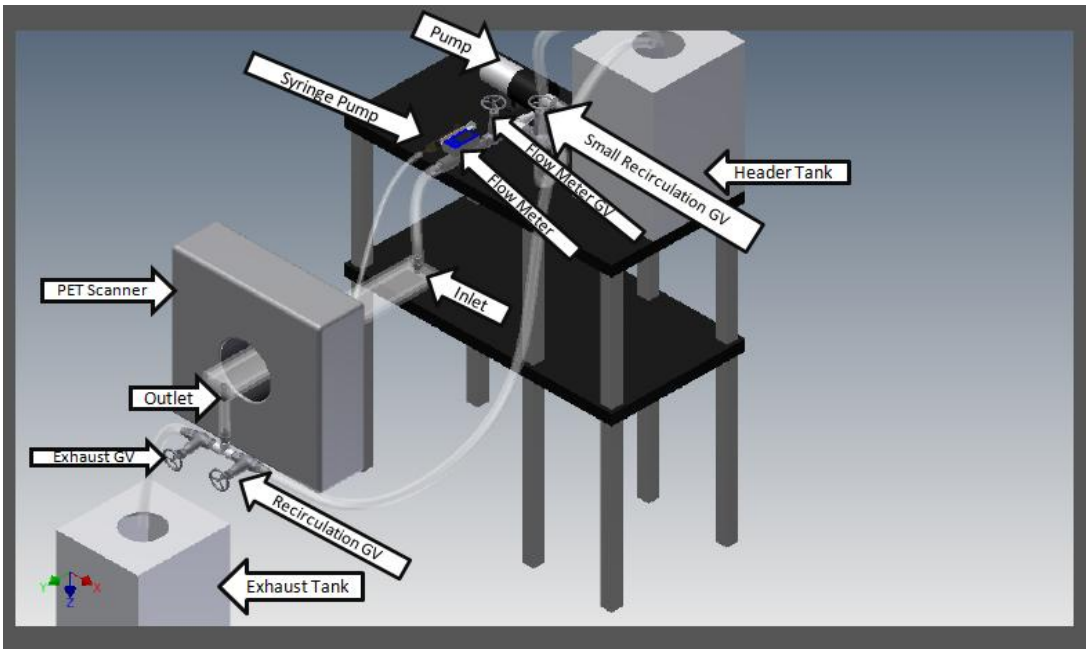

Figure 32: Proposed Hospital Setup

Figure 33: Header Tank and Control Box Identification

1. Place 7" piece of acrylic tubing in the PET scanner. . This will ensure that in the case of a leak the scanner will not get wet.
2. Secure the scanner bed to the scanner's maneuverable table Adjust the scanner bed to the desired position.
3. Place the test section on the bed and slide the test section through the bore of the scanner outlet end first.
4. Place a clamp on the end of the test section closest to the outlet. Place a clamp on each side of the test section 2 and 6 inches from the end of the test section at a 45 degree angle. Ensure that all clamps are over the gasket to provide optimum pressure for sealing.
5. Place the exhaust tank below the outlet.

6. Check that the gate valve on the header tank is closed. Fill the header tank with water. Use a dolly to transport the water-filled header to the cart.
7. Position the pump section and header tank on the top of the cart.
8. Unhook the piece of 3/4" tubing connected to the header tank from the loop of fishing line and attach it to the pump nozzle using a hose clamp.
9. Secure 3/4" tubing from recirculation gate valve to header tank using a hose clamp. Ensure the tubing is **NOT** submerged in the water.
10. Attach 1" tubing between the flow meter and test section inlet using hose clamps.
11. Attach 1" tubing between the test section outlet and the exhaust section using hose clamps.
12. Secure 1" tubing from exhaust recirculation gate valve to the header tank using hose clamps. Place a hose clamp on the end of the tub on the inside of the tube holder on the header tank so that the tube cannot come loose from the tank. Ensure the tubing **IS** submerged in the water.
13. Each tubing connection should be secured with a hose clamp. Double check all hose clamps.
14. Double check all connections.
15. Attach syringe tubing to the corresponding fitting in the test section. Ensure any extra fittings in the test section are tightly sealed.
16. Close the small recirculation and gate valve.
17. Check to make sure there are no kinks in any of the tubing. Monitor this issue the entire time the pump is running.

18. Connect the cart's power outlet to an extension cord.
19. Plug the pump into the cart's power strip.
20. Prime the pump.
    i. Open exhaust and recirculation gate valves
    ii. Open flow meter gate valve
    iii. Open header tank gate valve
    iv. Once water is flowing through the loop, plug the extension cord into an outlet outside of the scanner room (this turns on the pump).
21. Slowly close the exhaust valve and make sure no leaks are observed. If leaks are observed turn off the pump and open the exhaust valve to drain the system.
22. Use flow meter gate valve to adjust flow velocity to desired speed.
23. Connect the category 5 cable from the syringe pump to the left most port in the NanoJet control box (this corresponds to channel 1). The cat-5 cable is long enough to allow the control box to be set up and controlled from outside the scanner room.
24. Set desired settings on the NanoJet control box to inject particles into the test section.

**** Dose Begins, Less than 30 mCi F18 activity****

25. Place syringe in syringe pump and evacuate the scanner room. This may be done by the steady and experienced Alan Stuckey, or another

experienced with loading the syringe pump. This usually takes less than 30 seconds.

**** Dose Ends****

26. Start the NanoJet syringe pump injection.
27. **If there is a leak/spill at any point during the experiment after the syringe pump has discharged, de-energize the pump (this can be done from outside the scanner room) and evacuate the area for the remainder of the F-18 active lifetime. Normally return the next day and check activity levels.**
28. Initiate scan while the syringe pump injects particles.
29. Once data acquisition is complete, unplug the cart from the wall to shut off the pump.
30. Disconnect the cat-5 cable from the NanoJet control box.
31. Leave the system in the PET scanner room for 48 hours.
32. The following graph demonstrates the activity decay of F-18 over the 48 hours following the bead activation. The F-18 half-life is approximately 110 minutes and the activity decays as $A(t) = A_0 e^{-\lambda t} = 30 e^{\frac{-0.693t}{110\,mins}}\,mCi$. After 48 hours the activity decays to $3.83 \times 10^{-7}\,mCi$.

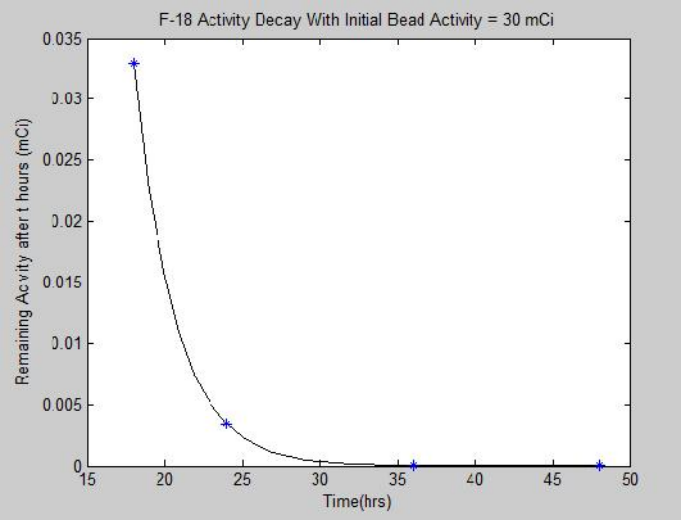

Figure 34: F-18 Activity Decay With Initial Bead Activity of 30mCi Over Time

Deconstruction:

33. Close header tank valve.
34. Remove the large recirculation tube from the water.
35. Open exhaust valve.
36. Open small recirculation valve.
37. Remove as much water from the loop as possible through the exhaust valve and into the exhaust tank. Pick up the pump, tubes, and any other loop pieces possible to let gravity help remove the water.
38. Empty header and exhaust tanks into the sink via their respective gate valves.
39. Lift up pump section above the height of the header valve and detach the 3/4" tubing from the pump only. Hang the tube in the loop of fishing line attached to the header valve to prevent dripping.

40. Remove pump recirculation tubing from the header and pump recirculation gate valve. Store the tubing.
41. Disconnect tubing from the pump section. Store the tubing and pump section.
42. Disconnect syringe tubing from the test section fitting.
43. Remove all the clamps upstream of the PET scanner from the test section **EXCEPT** the end clamp.
44. Pull the test section out of the back of the scanner enough to disconnect the tubing from the outlet without dripping any water in the scanner. Remove the tubing from the recirculation section and store.
45. Remove the test section from the scanner and empty any excess water in the sink.
46. Remove the rest of the clamps and the top. Dry off the test section.

End Protocol

Chapter 6

Conclusions

An experiment is designed suited to providing PIV data for a narrow rectangular channel flow. PIV data are collected in the channel and presented herein. The test section and attendant flow delivery systems are also designed for data collection using Positron Emission Particle Tracking (PEPT). A companion test is planned using a Siemens P4 preclinical scanner to collect PEPT data. Methods to compare the PIV data, which are snapshots of the velocity field in the channel from the laboratory reference, to the PEPT data, which are the particle trajectory in three dimensions as a function of time, are explored to facilitate a planned validation of the PEPT method performance. The direct comparison of the PIV measurement technique, the current standard for field velocity data in fluid flow, with the emerging PEPT method has never before been reported in the literature.

REFERENCES

[1] Todreas, N. E., & Kazimi, M. S. (2010). *Nuclear systems* (Vol. 1). CRC Press.

[2] Garratt, J. R. (1990). The internal boundary layer—a review. *Boundary-Layer Meteorology*, *50*(1-4), 171-203.

[3] Turbulence Intensity. (2012). Retrieved March 12, 2014, from http://www.cfd-online.com/Wiki/Turbulence_intensity.

[4] TSI (2011). INSIGHT 4G Data Acquisition, Analysis, and Display Software Platform
User's Guide. TSI Incorporated.

[5] Chaouki, J., Larachi, F., & Dudukovic, M. P. (Eds.). (1997). *Non-invasive monitoring of multiphase flows*. Elsevier.

[6] Bushberg, J.T., Seibert, J.A., Leidholdt Jr., E.M, Boone, J.M.. (Year). *The Essential Physics of Medical Imaging* (3rd ed.). City, St: Wolters Kluwer.

[7] Tapan K. Gupta author. *Radiation, Ionization, and Detection in Nuclear Medicide*. SpringerLink (Online service) Springer eBooks. Berlin, Heidelberg : Springer Berlin Heidelberg : Imprint: Springer, 2013

[8] "Positron Emission Tomography (PET) « Center for Molecular and Genomic Imaging." *Center for Molecular and Genomic Imaging RSS*. University of California Davis Biomedical Engineering College, n.d. Web. 19 Feb. 2014.

[9] Muehllehner, G., & Karp, J. S. (2006). Positron emission tomography. *Physics in medicine and biology*, *51*(13), R117.

[10] Chaouki, J., Larachi, F., & Dudukovic, M. P. (Eds.). (1997). *Non-invasive monitoring of multiphase flows*. Elsevier.

[11] Parker D. J., Forster R. N., Fowles P., Takhar P. S., *"Positron Emission Particle Tracking using the new Birmingham Positron Camera."* Nuclear Instruments and Methods in Physics Research, A 477, 540-545, 2002.

[12] Chu, G., & Tam, K. C. (1977). Three-dimensional imaging in the positron camera using Fourier techniques. *Physics in Medicine and Biology*, *22*(2), 245.

[13] Parker, D. J., & Fan, X. (2008). Positron emission particle tracking—Application and labelling techniques. *Particuology*, *6*(1), 16-23.

[14] Parker, D. J., Broadbent, C. J., Fowles, P., Hawkesworth, M. R., & McNeil, P. (1993). Positron emission particle tracking-a technique for studying flow within engineering equipment. *Nuclear Instruments and Methods in Physics Research Section A: Accelerators, Spectrometers, Detectors and Associated Equipment*,*326*(3), 592-607.)

[15] Buffler, A., Govender, I., Cilliers, J. J., Parker, D. J., Franzidis, J. P., Mainza, A., ... & Van der Westhuizen, A. (2009, May). PEPT Cape Town: a new positron emission particle tracking facility at iThemba LABS. In *Proceedings of International Topical Meeting on Nuclear Research Applications and Utilization of Accelerators* (pp. 4-8).

[16] Chang, Y. F., Ilea, C. G., Aasen, Ø. L., & Hoffmann, A. C. (2011). Particle flow in a hydrocyclone investigated by positron emission particle tracking. *Chemical Engineering Science*, *66*(18), 4203-4211.

[17] Boucher, D., Deng, Z., Leadbeater, T., Langlois, R., Renaud, M., & Waters, K. E. (2014). PEPT studies of heavy particle flow within a spiral concentrator.*Minerals Engineering*.

[18] Schaafsma, S. H., Marx, T., & Hoffmann, A. C. (2006). Investigation of the particle flowpattern and segregation in tapered fluidized bed granulators.*Chemical Engineering Science*, *61*(14), 4467-4475.

[19] Prasad, Ajay K., "Particle Image Velocimetry", *Current Science,* **79**, (2000).

[20] Keane, R. D., & Adrian, R. J. (1993). Theory of cross-correlation analysis of PIV images. *Flow visualization and image analysis*, 1-25.

[21] Crosskey, Mark W. "UTK Twin Jet Water Facility Computational Fluid Dynamics Validation Data Set." Master's Thesis, University of Tennessee, 2014.

[22] Schabacker, J., Bolcs, A.. *"Investigation of turbulent flow by means of the PIV method"*

[23] Corrsin, S. (1963). Estimates of the relations between Eulerian and Lagrangian scales in large Reynolds number turbulence. *Journal of the Atmospheric Sciences*, *20*(2), 115-119.

[24] Spydell, M. S., Feddersen, F., Guza, R. T., & MacMahan, J. (2014). Relating Lagrangian and Eulerian horizontal eddy statistics in the surfzone. *Journal of Geophysical Research: Oceans*.

[25] Wandel, C. F., & Kofoed-Hansen, O. (1962). On the Eulerian-Lagrangian transform in the statistical theory of turbulence. *Journal of Geophysical Research*, *67*(8), 3089-3093.

[26] "Positron Emission Tomography (PET) « Center for Molecular and Genomic Imaging." *Center for Molecular and Genomic Imaging RSS*. University of California Davis Biomedical Engineering College, n.d. Web. 19 Feb. 2014
Weinstock, J. (2008). Lagrangian–Eulerian relation and the independence approximation. *Physics of Fluids (1958-1988)*, *19*(11), 1702-1711.

[27] Zhang, Bi Yao, "Positron Emission Tomography (PET) for Flow Measurement. " Master's Thesis, University of Tennessee, 2011. http://trace.tennessee.edu/utk_gradthes/1042

[28] Hundsdorfer, W., & Verwer, J. G. (2003). *Numerical solution of time-dependent advection-diffusion-reaction equations* (Vol. 33). Springer.

[29] Chapter 5: Diffusion [PDF].(2014) Retrieved from http://www.physics.uwo.ca/~lgonchar/courses/p2800/Chapter5_Diffusion_Handouts.pdf.

VITA

Sarah Ridley Rupert was born on May 31, 1990. She attended the University of Tennessee Knoxville and earned her B.S. in Nuclear Engineering in 2011. She continued her education at the university and will earn her M.S. in Nuclear Engineering in 2014. This thesis serves as a part of the requirements for graduation from the M.S. program.